CHAPTER 3

RESULTS

The sensitivity of the Fabry-Perot resonator can be used to detect changes in the shape, size and, refractive index of cells flowing through the microfluidic channel. When a cell, or any other micro-sized body crosses the resonator it perturbs the fringe pattern. This chapter shows how to detect, acquire, and process the perturbation to extract meaningful information about cells' optomechanical properties.

3.1 Fabry-Perot resonator fringe pattern analysis for cytometry

The analysis of the cell-induced fringe pattern perturbation allows us to retrieve the cell's optomechanical properties. First, we present a detailed description of the observed perturbation types, together with the relevant parameters. Next, we show the related information about the Cell-Induced Fringe Pattern Perturbation (CFPP) and its extraction from the experimental data, followed by computational and statistical analysis. Finally, we discuss the computed values for CFL and Finesse for the following samples: Saccharomyces cerevisiae (yeast), tetraselmis (algae), 3 μm diameter polystyrene beads, and 15 μm diameter microgel beads (which mimic cell mechanical properties [36]).

3.1.1 Acoustofluidic channel Fabry-Perot fringe pattern

As shown in Section 2.1, an interferometric cavity surrounds the microfluidic channel. The laser beam coupled into the empty cavity (i.e. devoid of cells) produces the Resonator Fringe Pattern (RFP), shown in Fig. (3.1) and mathematically described by the Airy function (eq. (1.15)). The Gaussian beam's waist diameter, focussed by the microscope objective, is marked by the yellow bar in the center of the concentric circles (Fig. (3.1)), highlighting the interaction region around the interferometer's axis.

3.1.1.1 Interferometer's Fringe Pattern stability

Since Fabry-Perot's resonator reflective surfaces are the planar glass plates that define the microfluidic channel, the interferometer is highly sensitive to temperature gradients and hydrostatic pressure from

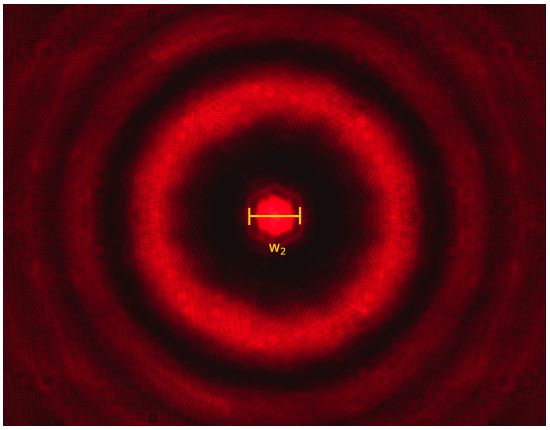

FIGURE 3.1. Fabry-Perot's resonator fringe pattern Resonator Fringe Pattern (RFP). The focussed laser's beam waist is $w_2 \approx 4\mu$m.

the induced flow. The latter is controlled by two syringes (as reservoirs): in the measurement, the liquid level in the syringes changes and, with it, the particle speed and the pressure inside the channel. The resonator's fringe pattern can be affected by the acoustic wave amplitude change which manipulates the cells inside the channel. All these effects contribute to change the order of interference m, inducing a shift in the concentric circles observed in the RFP, which remains constant only for short periods (from seconds to minutes, depending on condition). This slow drift must be taken into account to avoid biasing the data analysis.

3.1.2 Weak and strong perturbations of the cell-induced fringe pattern

The intensity of the observed perturbation strongly depends on the cell's position (x, y, z) inside the Fabry-Perot cavity. A strong perturbation occurs when the cell crosses the Fabry-Perot resonator axis $(0, 0, z)$. In this position, light impinges on the cell at normal incidence, equivalent to a maximum phase shift, $\alpha = 0$ (cf. Section (2.3.1)): examples are shown in Fig. (3.2) (b), (d). In contrast, when cells do not cross the axis $(x, y \neq 0)$ the angle of incidence is oblique, reducing the interference pattern perturbation to a weak RFP local modification, more difficult to identify (Fig. (3.2) (a), (c)).

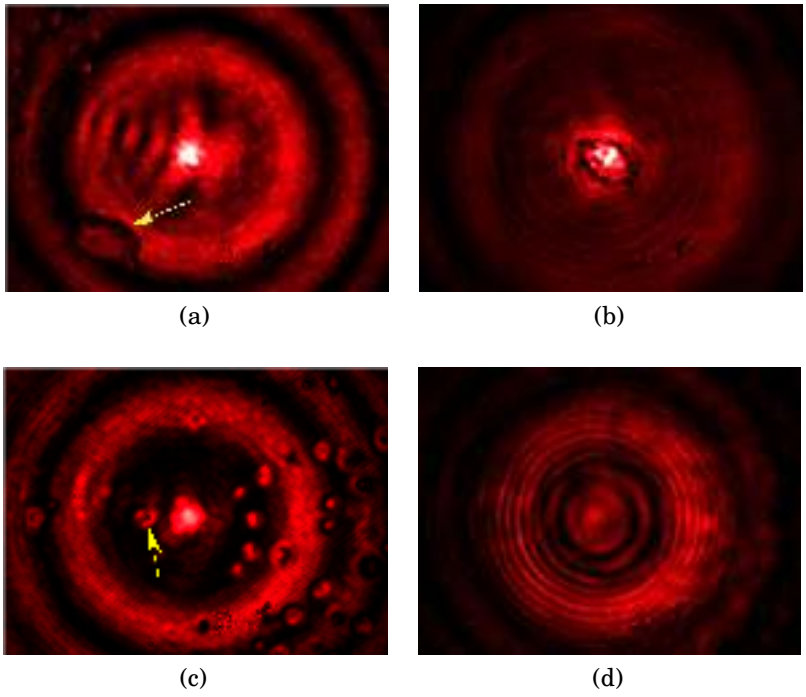

(a) (b)

(c) (d)

FIGURE 3.2. Panel (a): non-perturbed resonator fringe pattern with an algae cell in the lower-left corner (oval shape) and yeast cells in the upper left corner (small spheres). Panel (b): RFP perturbation caused by the algae cell previously shown in panel (a) but is now placed in the center of the fringe pattern's concentric circles. Panel (c): yeast cells weakly interacting with the background fringe pattern. Panel (d): yeast-induced strong perturbation of the fringe pattern (as in panel (c)), placed in the center of the resonator's fringe pattern concentric circles. The yellow arrows mark the objects of interest in panels (a: algae) and (c: yeast). The fringe pattern of the low finesse Fabry-Perot resonator is recognizable in the background of all panels.

On the other hand, the observation coordinate z influences the magnification of the imaged interference pattern. Setting the focal plane defined by the microscope objective at $(x, y, 0)$ – i.e., on the plane of maximum acoustic power – a focussed but minimally magnified virtual image of the perturbation will be observed, while at $(x, y, \pm z_m)$ (with $z_m = 35\,\mu$m for our experimental setup (cf. section (2.1)) an ideal magnification of the perturbation will be appreciated. In other words, the fringe pattern is best visualized (Fig. (3.3)) when the cell is not in the objective's focal plane [81].

3.1.2.1 Cell acoustic impedance

Cells have different acoustic impedance due to their different sizes and densities, together with the gravitational effect, causes that different cell type to lie at different planes for the same acoustic force amplitude [25, 110] (cf. Fig. (1.11)). The different responses, if significant, will be detected by the device. Thus, applying different acoustic focussing forces to different samples will result in possibly wrong classifications.

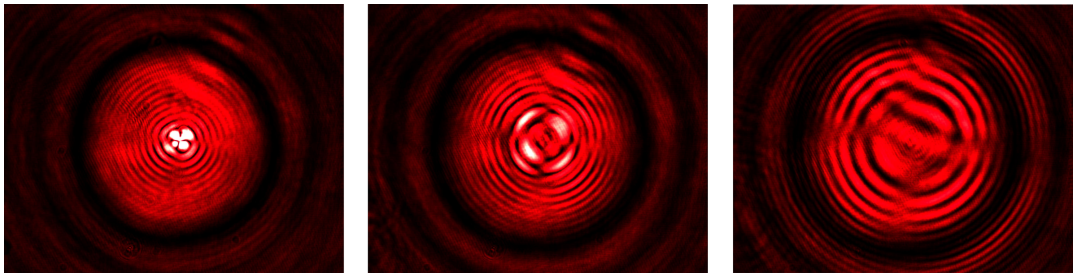

FIGURE 3.3. Polystyrene 3 μm diameter at different focal planes. The fringe pattern's different sizes imply that images are acquired different optical planes; in focus, $z = 35\,\mu$m and $z = 40\,\mu$m, from left to right, respectively.

3.1.2.2 In-flow cells' population density

Ideally, only one cell should be present in the strong interaction area at any time (resonator's beam waist region around the optical axis), to best detect its induced perturbation on the fringe pattern. This determines the cell flow and the resulting density of cells in the camera's FOV for any given camera frame rate. With the current parameters of our experimental setup, a good compromise to maximize throughput while fulfilling the previous condition amounts to 3–4 $\times 10^8$ cells/ml, i.e., $\approx$ 20 cells simultaneously present in the camera FOV. Future versions of the AID will include lateral acoustic focusing, enabling one single line of motion instead of one motion plane, allowing for working with much lower cell counts.

3.1.3 Measuring the FP perturbation

All of our following results are based on strong CFPP observations. As we can observe from the previous section the RFP and the CFPP are composed of concentric circles, thus possess polar symmetry. A plot of the intensity profile over any of the radial lines of a CFPP image will be useful to measure the FSR and the FWHM (cf. Fig. (3.4)), which can be used to compute the Finesse (cf. Fig. (1.2)). A detailed analysis of the statistical significance of the CFPP's 2D information is performed with the acquired images. Temporal traces also allow for a 1D quasi-real-time analysis of the CFPP. Details about this operation mode of the AID (based on the photodiodes detectors) will be discussed in the next chapter.

3.1.3.1 Different cells induce different CFPP

A comparison of the resonator fringe pattern and the resonance induced by yeast, algae, and polystyrene beads is shown in Fig. (3.5). The polar symmetry of the CFPP permits the extraction of the intensity profile by plotting the intensity over a straight line that passes through the center of the image (resonator's axis). A reduction in background intensity is observed in the presence of the cell, clearly visible by comparing the RFP and CFPP intensity profiles (Fig. (3.5)) in the pixel range 0–500 and 1500-2000.

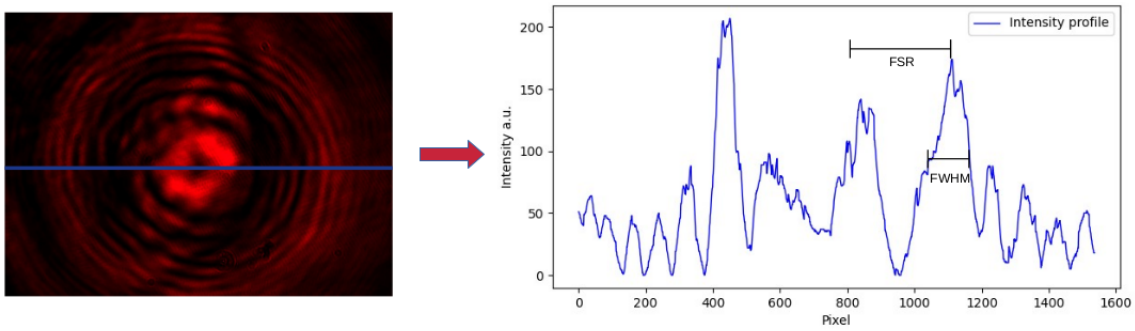

FIGURE 3.4. The CFPP intensity profile is created by plotting the intensity in the images over a virtual horizontal (blue) line passing through the center of the image. The relevant measurement parameters are also presented: the separation between adjacent maxima, or FSR, and the FWHM of the peaks.

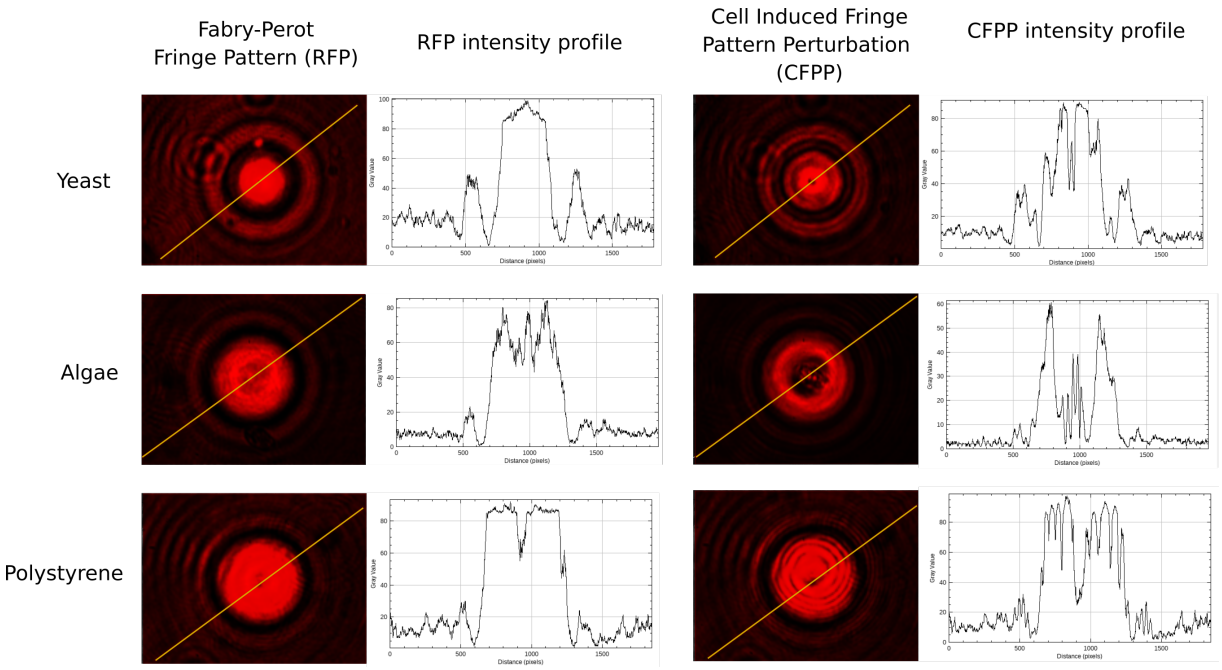

FIGURE 3.5. In the upper, middle and lower rows, panels present the RFP and the CFPP for yeast, algae, and polystyrene, respectively. The left column shows the resonator fringe pattern just before a cell enters the optical cavity. The yellow line is a cut through the pattern over which the RFP intensity profile is plotted. The second column shows the intensity profile of the RFP along the yellow line. The third column shows the cell-induced fringe pattern perturbation, with the corresponding yellow line for the intensity cut shown in the fourth column.

Visual inspection shows that the perturbation introduced by polystyrene is more easily identified than the one due to yeast or algae, thanks to its higher refractive index contrast ($n_{poly} = 1.55$, $n_{water} = 1.33$).

Cells, instead, have a refractive index that can hardly be higher than 1.4 because they are mainly composed by water. Comparing the profiles to the matching RFP (due to the resonator's sensitivity to external conditions) one notices the presence of a set of fine peaks which appear in the center of the algae plot, surrounded by two large, broad peaks; instead, the yeast's CFPP intensity profile is more uniform, devoid of fine peaks. The appearance of fine peaks is attributed to the comparatively larger size or inner structure of algae cells that contribute high-frequency spatial components to the spectrum. Instead, the much smaller yeast cells contribute lower frequency components that are not necessarily resolved on top of the interference pattern.

These considerations are heuristic and are presented for illustration purposes. Quantitative information is needed and is extracted from the CFPP analysis presented in the next section to extract the cell's optomechanical properties through CFL and Finesse. The computational automation for CFPP analysis shown in the next section.

3.2 Cell induced fringe pattern perturbation images: statistical analysis

360 intensity profiles are possible to obtain from each of the images of the CFPP, enabling robust analysis of the acquired data. In this section, the method used to complete this task is presented. First, the images are converted to polar coordinates to obtain the 360 intensity profiles. Then, the profiles are computationally analyzed to obtain the relevant parameters: ρ, FWHM and FSR and to execute an outlier elimination, thus improving the normality of our dataset. Finally, a weighted average of the aforementioned parameters is performed therefore to obtain the final result.

3.2.1 Polar representation of the CFPP images

As shown in section (3.1.3) the intensity profiles can be plotted over any of the radial lines $\alpha = c$ corresponding to the diameter of the concentric circles of the RFP. An angle increment of 1° enables the analysis of 180 diameter intensity profiles (or 360 radius profiles) present in the polar symmetric CFPP. For instance, the reference intensity profile in Fig. 3.6 (a) – blue line – has been plotted over the radial line $\alpha = 0°$ (Fig. (3.6) (b)), while the reference intensity profile has been plotted over the radial line $\alpha = 45°$ (Fig. 3.6 (c)). To exploit the polar symmetry of the CFPP, acquired images are transformed into polar coordinates utilizing the `scikit-image` warp_polar function [106] (cf. Fig. (3.7) (a)).

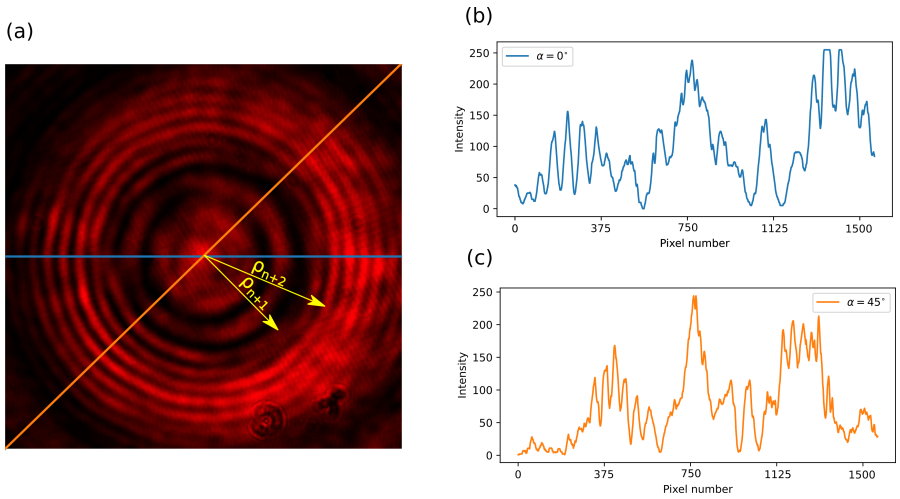

FIGURE 3.6. (a) Vectors ρ_{n+1} and ρ_{n+2} identify the distance between the resonator's axis and consecutive constructive interference fringes in yeast's CFPP. (b) and (c) display the intensity plots obtained from the image cut through the blue and orange lines, respectively.

The intensity profiles over the radial lines for $0 \leq \alpha < 180°$ are represented in 360 horizontal lines in Fig. (3.7) (a). Since the polar representation permits the split of the diameter intensity profiles into radial ones; for instance, the interval from 0 to 750 in the x-axis of Fig. (3.7) (b) will be represented in line 0 of the polar transformation. In contrast, the interval 751 to 1500 will be represented in line 180. The 360 profiles are retrieved and automatically analyzed as presented in the next section. e increment from 1 to 360 CFPP intensity profiles allows for statistical processing of the interesting parameters: FWHM, FSR and ρ.

3.2.2 Automation of the fringe pattern analysis

We have implemented an automatic analysis of the CFPP image intensity profiles. A Python script allows for the profile's peaks identification and the measurement of the peak's position and FWHM. The computational algorithm is based on the Savitzky−Golay Filter (SGF) data filtering followed by the implementation of the `find_peaks` function.

3.2.2.1 Savitzky-Golay filter

The intensity profiles are filtered with the help of the SGF from the Scipy library. This digital filter is applied to a set of digitized points to smooth the noise superposed on the data. Its function is to remove unnecessary details without altering the original functional shape. This is achieved by fitting successive subsets of adjacent data points with a low-degree polynomial using a linear least-squares method. When the data points are equally spaced, an analytical solution to the least-squares equations can be found [90].

3.2.2.2 Scipy `find_peaks` function

The `find_peaks` function allows for peak identification using several parameters [107]; Prominence and Height are used in this work. The prominence value P_v establishes a minimum height value – measured from the surrounding data [107] – required for a protuberance to be counted as a peak. The height values H_v is the y-axis threshold that the data have to overcome to be considered as a peak. This function returns the position, height, and width of all the peaks that match the criteria of Prominence and Height.

3.2.3 Polar representation alignment

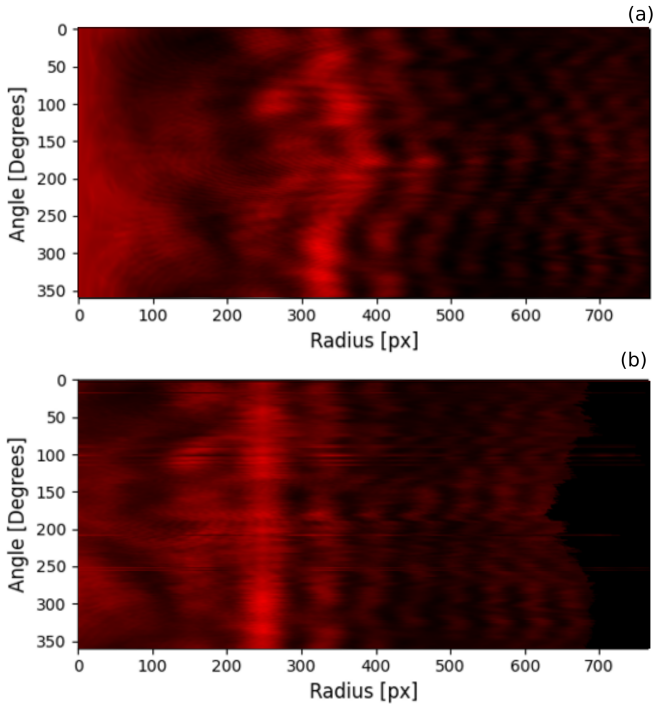

FIGURE 3.7. Yeast-Cell-Induced Fringe Pattern Perturbation image transformed to polar coordinates (a). Alignment of the polar profile (b) to accurately measure the ρ value of the largest four bright fringes.

The wavy structure in Fig. (3.7) (a) comes from the (slight) misalignment between the resonator's axis and the cell CFPP, leading to a misalignment between the identification of the resonator's axis and the true one around which the CFPP emerges. To eliminate this effect, the `find_peaks` function is used to find the peaks in the intensity profiles of Fig. (3.7) (a). The parameters of the `find_peaks` function are: $H_v = y_{\text{av}}$ where y_{av} is the average of the maximum and minimum value in the intensity profile, while the software automatically sets P_v until the four largest peaks are found. We noticed that at least four well-defined peaks can be found in all the CFPP of our samples.

The `find_peaks` function reads the data from left to right and saves the found peaks in an ordered array where the leftmost value is the first peak and the rightmost the last one. The position of the first peak of the 360 intensity profiles is determined, and then the minimum value ρ_{min} is computed. Next, all the intensity profiles in the polar transformed image are shifted horizontally align with the first peak. This way, the CFPP structure can be aligned (cf. Fig. (3.7) (b)).

Once again, the `find_peaks` function is used to find the largest four peaks and to retrieve their position, height, and width in the aligned image. The measured ρ_n values are now used to compute the CFL (cf. section (2.4.1.1)). It is important to notice that the shift applied to the polar transform indeed affects the actual ρ_n values. Nevertheless, since the parameter needed to compute the CFL is the $\Delta\rho = \rho_{n+1} - \rho_n$ the shift does not influence the remainder of the calculation, the aliment is of relevance when an average over

the angle α of the fringe pattern is computed. Similarly, the FSR and the FWHM, calculated from the relative peak position and width, are invariant under the shift, leaving the Finesse unaffected.

3.2.4 Fringe pattern statistical distribution

Twenty images with cells are acquired for each sample (yeast, algae, polystyrene, and microgel). Next, the images are converted to polar coordinates and computationally analyzed as described in the previous section. The values ρ, FSR and FWHM of the two largest peaks are used for the computation and for the statistical analysis of the cell's Finesse and CFL. The choice of using just the two first peaks is justified by the fact that they are the best-defined (cf., e.g., the bright fringes at $\rho_1 = 250$ [px] and $\rho_2 = 330$ [px] in Fig. 3.7 (b)).

The dataset of the fringe pattern's radial position of the first two fringes ρ_1 and ρ_2 are saved in a .csv file, useful to plot a density histogram of ρ_1 values (blue histogram in Fig. 3.8) where a Gaussian curve (shown in blue) has been fitted directly to the data (not to the histogram) to obtain the data's mean value and standard deviation, thus revealing the presence of an outlier-induced heavy-tailed distribution.

3.2.5 Outlier elimination

Artifacts – incorrect peak identification, background noise, and poor CFPP contrast – may lead to outliers in the ρ data set distribution. In Fig. (3.8), the distances that lay in the range [0, 20] are obvious outliers and should not be considered. For instance, the horizontal blurred lines in Fig. (3.7) (b) (present in the angle values of 100° and 250°) are due to the first peak's wrong identification. This is one of the artifacts that contribute to outliers.

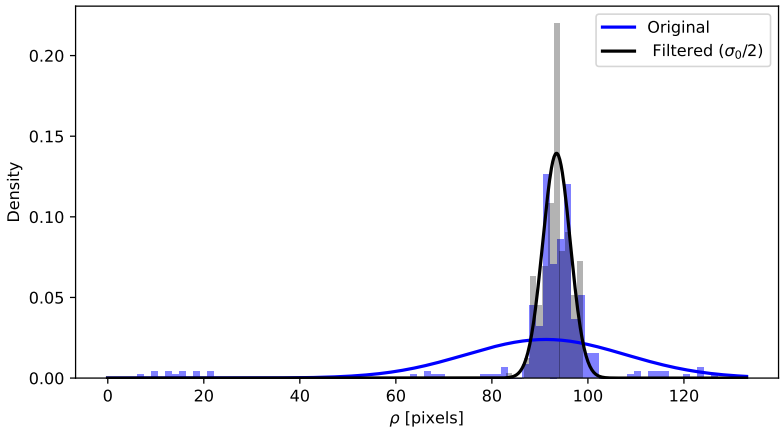

FIGURE 3.8. Density histogram (blue bars) of the ρ_1 values in the original data (first peak from the CFPP reconstructed center). The blue line is the Gaussian fit to the original data (applied directly, rather than on the histogram). Gray bars correspond to the density histogram of the filtered data. The black line corresponds to the Gaussian fit of the filtered data. Parameters: $\mu_0 = 91.20$, $\sigma_0 = 16.66$, $k_{s,0} = 14.65$ (excess kurtosis) and $G_{1,0} = 294.04$ (skewness) for the original data; $\mu = 93.46$, $\sigma = 2.86$, $k_s = -0.14$ and $G_1 = 8.18$ for the filtered data.

To remove the outliers, the data were filtered as follows:

$$V_f = \{x \epsilon V \mid \mu_0 - \sigma_0/2 \leq x \leq \mu_0 + \sigma_0/2\}$$

where V is the original ρ_1 data set (with μ_0 and σ_0 the corresponding mean value and standard deviation) and V_f the filtered dataset.

The normality of the ρ dataset was tested before and after filtering through the computation of Kurtosis and Skewness. Skewness measures the left-right symmetry around the center point, while kurtosis quantifies the distribution's tails weight compared to the normal distribution. Large values of kurtosis correspond to the presence of heavy tails (outliers) while – as detailed below – low kurtosis indicates excessively peaked distributions.

3.2.5.1 Skewness

For univariate data $x_1, x_2, \ldots, x_N$ the formula for skewness is [39]:

$$g_1 = \frac{\sum_{i=1}^{N}(x_i - \mu)^3/N}{\sigma^3}, \tag{3.1}$$

where μ is the mean, σ the standard deviation, and N is the number of data points. The above formula for skewness is referred to as the Fisher-Pearson coefficient of skewness. However, we prefer computing the adjusted Fisher-Pearson coefficient of skewness [39]:

$$G_1 = \frac{\sqrt{N(N-1)}}{N-2} \frac{\sum_{i=1}^{N}(x_i - \mu)^3/N}{\sigma^3}. \tag{3.2}$$

The adjustment approaches 1 as N grows large. For reference, the adjustment factor is 1.49 for N = 5, 1.19 for N = 10, 1.08 for N = 20, 1.05 for N = 30, and 1.02 for N = 100. In our case, data points are 360 and at least 180 for the filtered data set, so the adjusted and normal Fisher-Pearson coefficients match.

The skewness for a normal distribution is zero, and in practice, any symmetric experimental data should have a skewness near zero. Negative values for the skewness indicate data that are skewed left, and positive values for the skewness indicate data that are skewed right of the maximum.

3.2.5.2 Excess kurtosis

For univariate data $x_1, x_2, \ldots, x_N$ the formula for kurtosis is [39]:

$$\mathrm{k_{s1}} = \frac{\sum_{i=1}^{N}(x_i - \mu)^4/N}{\sigma^4}. \tag{3.3}$$

The kurtosis for a standard normal distribution is three. For this reason, we use the following definition of kurtosis (often referred to as "excess kurtosis"):

$$\mathrm{k_s} = \frac{\sum_{i=1}^{N}(x_i - \mu)^4/N}{\sigma^4} - 3. \tag{3.4}$$

This definition is used so that the standard normal distribution has $k_s = 0$. This way, positive excess kurtosis indicates a "heavy-tailed" distribution, and a negative one identifies a "light-tailed" distribution.

In Fig. (3.8) the skewness of the data set is reduced from 294 to 8, going from a heavily asymmetric distribution to a (nearly) symmetric one. The excess kurtosis goes from 14.65 (heavily tailed) to -0.14, resulting in a slightly light-tailed distribution, thanks to the outlier elimination. Filtering produces a (nearly) normal dataset distribution, reducing the standard deviation $\sigma_0 \rightarrow \sigma$ and preserving the mean value μ. This process enables more accurate measurement of the ρ parameter, with a smaller error. The outlier elimination procedure was applied for ρ_1 and ρ_2 to all the CFPP images for yeast, alga, microgel, and polystyrene. The retrieved data was then used to compute the CFL and the Finesse, which is useful for discriminating cells samples types and studying acoustically-induced deformability.

3.3 Cells' acoustic pressure response

Acoustic focusing is achieved thanks to the piezoelectric transducer, whose frequency is set at the resonance frequency ν_R and voltage at the focusing voltage amplitude V_f (cf. section (2.1.2)). Once a cell was aligned with the resonator's axis, the flow inside the microfluidic channel was stopped. With the cell acoustically focused in the resonator's axis region, an image of the CFPP was acquired. Then, in order to induce a significant acoustic pressure, the voltage was increased to reach the deformation voltage V_d and a second image of the perturbation of the same cell was acquired. Next, the acoustic pressure was reduced again to V_f and the flow was reintroduced to repeat the process for another cell. This process was repeated 20 times to obtain 20 images of the CFPP at V_f and 20 images of CFPP at V_d of the same sample. This procedure was carried out for each of the available samples: yeast, algae, microgel (μgel) beads, and polystyrene.

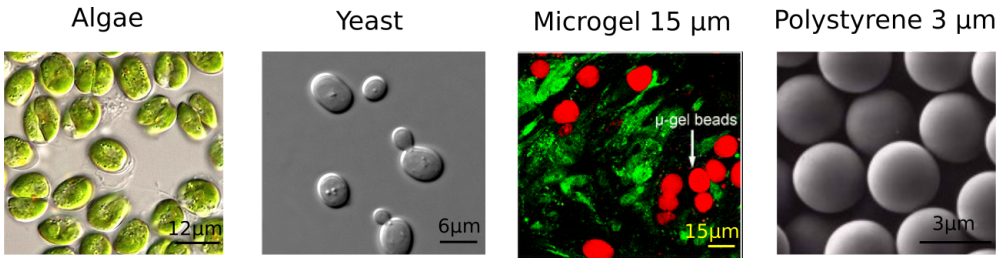

FIGURE 3.9. Images of the samples. The scale changes from one image to the next for clarity.

The outlier elimination was implemented as described in subsection 3.2.5. With the filtered data, an ANOVA test [1] was applied to the measured ρ_1, ρ_2, FWHM_1, and FWHM_2 acquired at V_f and V_d to determine the existence of a statistically significant difference. The results are shown in table (3.1).

Cell	ANOVA P-value			
	ρ_1	ρ_2	FWHM_1	FWHM_2
Algae	.027	.016	.085	.111
Yeast	.449	.290	.192	.139
Microgel	.734	.987	.264	.236
Polystyrene	.372	.888	.210	.895

TABLE 3.1. ANOVA analysis of the ρ_1, ρ_2, FWHM_1 and FWHM_2 for CFPP of the samples with two different acoustic pressures V_f and V_d , matching the indices 1 and 2, respectively.

The results of Table (3.1) allow for a comparison of the acoustically induced changes on the measured parameters: ρ and FWHM, for each of the samples (after outlier elimination). For the biological samples, ρ_2 changes more than ρ_1 while for microgel and polystyrene, the opposite is true. For the FWHM, it is not possible to establish a general behavior. The position (ρ_2) and width (FWHM_2) of the polystyrene's second bright fringe do not undergo a statistically significant change. Among all the samples, algae measured parameters are significantly different in a statistical sense, cf. Table (3.1). Thus, an evident change in the alga's CFL and Finesse is expected, while the change of the polystyrene's parameters is expected to be non-existent.

After computing the ANOVA test of the measured parameters dataset, a weighted average of the ρ_1, ρ_2, FWHM_1, and FWHM_1 values (after outlier elimination) is carried out. The results are used to compute the Finesse (eq. (1.23)), the CFL (eq. (2.81)) and the error propagation (cf. section (2.4.2)); such results are shown in Figs. (3.10) and (3.11). The statistically significant difference of the results is also analyzed, but this time using the Student's Tests (T-test) [8].

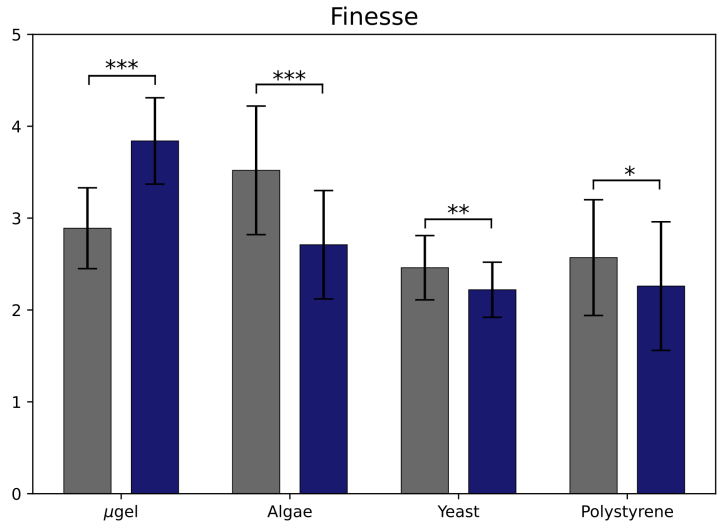

FIGURE 3.10. Finesse values for Saccharomyces cerevisiae (yeast), tetraselmis (algae), microgel beads 15 μm diameter, and polystyrene beads 3 μm diameter. Gray bars represents acoustic focusing (V_f = 15 V_pp), while blue bars display the results for acoustic deformation (V_d = 25 V_pp). The asterisks in the plot indicate: *** P< .001, ** P< .05 and * P> .1. The P-scores were computed from the samples T-test results with the following scores: μgel = -6.59, Algae = 3.95, Yeast = 2.33, and Polystyrene = 1.51.

When computing the CFL two possible solutions can be obtained from the roots of the second-degree equation found in section (2.4.1.2). The positive root of the eq. (2.77) was chosen as the computed CFL since this value is more sensitive to the change induced by the cell presence and is less prompt to the errors introduced by the experimental setup (cf. sect (2.4.2.2)). It is also important to notice that the negative value of the CFL originates from the negative curvature solution of the wavefront exiting the resonator (i.e., a concave shape in the direction of propagation of the wave exiting the resonator).

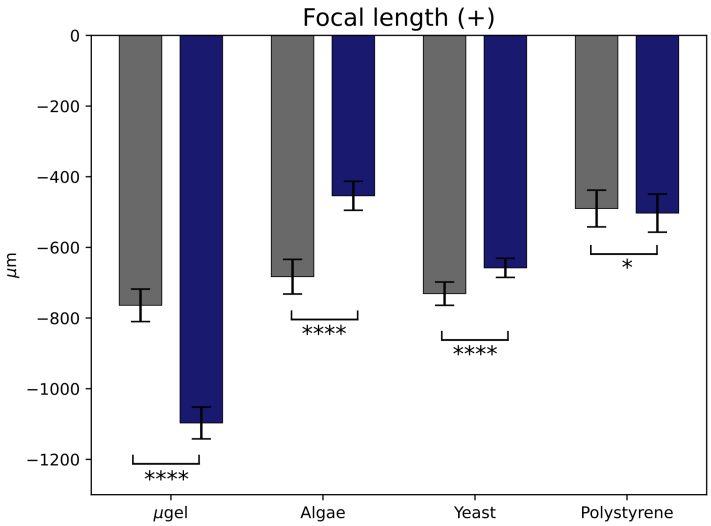

FIGURE 3.11. Cell Focal Length values for Saccharomyces cerevisiae (yeast), tetraselmis (algae), microgel beads 15 μm diameter, and polystyrene beads 3 μm diameter. Gray bars represents acoustic focusing ($V_f = 15\ V_{pp}$), while blue bars display the results for acoustic deformation ($V_d = 25\ V_{pp}$). The asterisks in the plot indicate: **** $P < .0001$, and * $P > .1$. The P-scores were computed from the samples T-test results with the following scores: μgel = 22.88, Algae = -15.98, Yeast = -7.56, and Polystyrene = 0.79.

The Finesse, bar plot Fig. (3.10), and the CFL, bar plot Fig. (3.11), show an acoustically-induced cell deformation for yeast and algae. A drop in the Finesse and CFL values is also observed. For the microgel beads an acoustic effect is observed, but, contrary to the biological cells, it increases both Finesse and CFL. The polystyrene beads, instead, do not present a significant deformation. This is consistent with their large Young modulus 3.25 GPa. For comparison, the Young modulus of the microgel beads amounts to 1.7 kPa [36], while the maximum expected applied pressure in a similar configuration of our device is $\approx$ 15kPa [75]. The expected cell wall's Young modulus for yeast is (112 ± 6) MPa [94]. The algae don't have a special cell membrane or special cytoskeleton structure, they are expected to be elastically rather compliant. The order of our samples is expected to be (from the most to the least elastically compliant): microgel beads, algae, yeast, and polystyrene beads. This order matches our results.

3.4 Chapter summary

When an acoustically focused cell crosses the Fabry-Perot cavity of the AID it will perturb the resonator fringe pattern, governed by the Airy transmission function (cf. section (1.1.1)). We have identified two types of cell-induced perturbations: strong and weak. The strong perturbation occurs when the cell crosses the resonator's axis, while the weak perturbation will occur when the cell crosses any other section of the resonator (cf. section (3.1.2)). The strong perturbations are better defined and are easier to observe. The results presented in this chapter are based on the strong cell-induced fringe pattern perturbations referred to as CFPP.

As stated in the previous chapter, the parameter used to quantify the CFPP are the CFL and the Finesse, computed from the ρ, FWHM, and the FSR. Images of the CFPP are acquired with the AID; intensity profiles are obtained from the images to measure the ρ, FWHM, and the FSR parameters (cf. section (3.1.3)).

360 intensity profiles can be obtained from each of the images of the CFPP, enabling statistical analysis of the acquired data. First, the images are converted to polar coordinates to obtain the 180 independent intensity cuts through the image. Then, the profiles are computationally analyzed to obtain the parameters: ρ, FWHM, and FSR. An outlier elimination procedure is implemented to improve the normality of our dataset. Finally, a weighted average of the aforementioned parameters is performed to obtain the final result (cf. section (3.2)).

The experimental procedure used to obtain the interference patterns produced by the cells in the absence and the presence of mechanical deformation is the following. The flow inside the microfluidic channel is stopped when a cell is aligned with the resonator's axis (while acoustically focussed). The immobile and levitated cell's interference pattern is acquired, obtaining the information in the absence of deformation. Then, the acoustic wave's amplitude is increased to induce a cell deformation and a new image of the interference pattern is acquired. The cycle is repeated to obtain 20 pairs of patterns in the absence and in the presence of cell deformation.

With the filtered data, an ANOVA test was applied to the measured ρ_1, ρ_2, FWHM_1 and FWHM_2 acquired with and without deformation to determine the existence of a statistically significant difference. A weighted average of the ρ_1, ρ_2, FWHM_1 and FWHM_1 values (after outlier elimination) is carried out.

Next, a weighted average of the ρ_1, ρ_2, FWHM_1 and FWHM_1 values is performed. The results are used to compute the Finesse (eq. (1.23)), the CFL (eq. (2.81)) and the error propagation (cf. section 2.4.2); the corresponding results are shown in Figs. (3.10) and (3.11). The statistical significance of the resulting estimates is analyzed with Student's T-test. Results show an acoustically-induced cell deformation for yeast and algae. A matching diminishing in the Finesse and CFL values is also observed. The polystyrene beads, instead, do not present a significant deformation. The absence of measured deformation proves that the system works correctly. Thus, offering a corroboration of the working principle behind the AID.

CHAPTER 4

DISCUSSION AND CONCLUSION

With the AID, we introduce an Acoustofluidic Interferometric Technique (AIT) capable of detecting subtle deformations in the cell when acoustic pressure is applied. The relatively low magnitude of the used acoustic pressure in this work doesn't allow to observe cells' deformation with standard microscopy instruments. Still, it is possible to observe and measure cells' acoustically-induced deformations thanks to the AID through the Finesse and the Cell Focal Length. Based on the results presented in chapter 3 it is possible to remark that the AIT can perform label-free cytometry using the optomechanical properties of the cells as biomarkers in a novel way. In this last chapter, we discuss optimizing the device's geometry, and the quasi-real-time implementation of the AIT. Finally, we identify the technology's potential applications.

4.1 Device analysis

An analysis of the AID chip geometry is presented in this section. This analysis is useful to design new versions of the AID with geometric parameters that improve its performance. Also, we critically analyze the thin lens approximation to model the cell's influence on the interference pattern. This analysis concludes that the approximation holds for all the expected cell kinds. Its validity was expected from the general considerations offered in Section 2.4.1. Still, it was also imposed by the complexity of modeling a thick lens inside the cavity with the ray matrix formalism. While the thin lens representation gave rise to quadratic expressions for the equivalent focal length, the thick lens one produced an equation of eighth-order, with all the difficulties it entails. One would be obliged to solve it numerically, without a way of computing the errors – contrary to what we have done in section (2.4.2.2). In addition, the number of physically relevant solutions would be in principle unknown and their pertinence to the problem. Moreover, in the next section, we will show that the thin lens approximation is adequate to assess the optomechanical properties of the cells, and the thick lens approximation is not required.

4.1.1 Back mirror thickness effect on the CFL

By plotting the CFL eq. (2.81) vs. the back reflecting mirror thickness, eq. (2.53), it is possible to remark that its variation with respect to t_m is nonlinear (Fig. (4.1)).

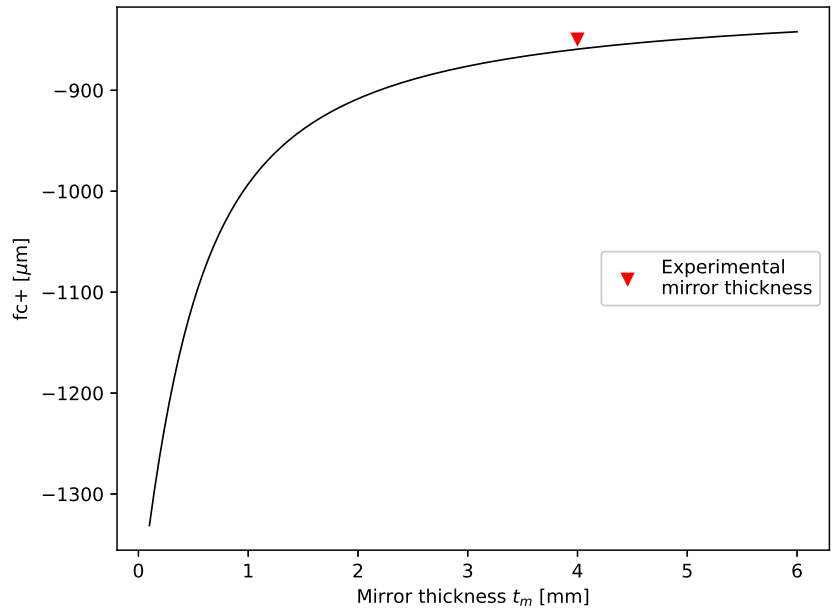

FIGURE 4.1. A plot of the CFL eq. (2.81) vs. mirror thickness t_m eq. (2.53). A hyperbolic dependence of $f_{c,+}$ on back mirror thickness t_m is observed. The remaining parameters are held constant: $R_{in} = -9mm$ – incoming beam's – and $R_{out} = 11mm$ – outgoing beam's radii of curvature, respectively –, $L = 106mm$ – microfluidic channel width –, $t_m = 170\mu$m – coverslip thickness (wall 1 of the device).

It is interesting to notice that the CFL depends on the back mirror thickness. Smaller values for the mirror thickness would facilitate the observation of changes in the CFL. Thus, using a front surface, rather than a back surface, mirror would provide ideal working conditions for our device. Instead, a back-mirror thickness larger than 5 mm would significantly reduce the CLF measured, considerably decreasing the instrumental sensitivity and potentially leading to incorrect cell assignments. The 4 mm back mirror thickness used in the device does not reduce significantly the sensitivity of the AID.

4.1.2 Channel width effect on the CFL

Standard channel widths (L) for microfluidic channels with acoustic cell's manipulation vary from 100 μm (like ours) to 300 μm (like the one in [118]). In Fig. (4.2) we observe a linear dependence of CFL on microfluidic channel thickness L. The linear function has very small slope (m$= 4 \times 10^{-3}$ cf. Fig. (4.2)). Thus, the channel thickness does not substantially influence the CFL, while wider channels permit the use of lower resonance frequencies for cell acoustic manipulation. Lower frequencies are easier to generate with commercial generators, useful when simplifying the implementation of the acoustic manipulation.

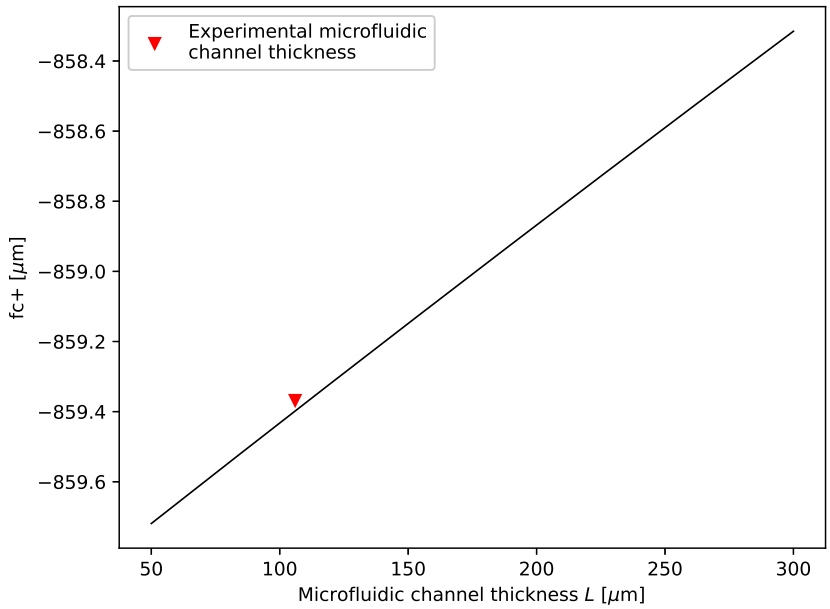

FIGURE 4.2. A plot of the CFL, eq. (2.81), vs. the microfluidic channel width L, eq. (2.52). All other parameters were kept constant: $R_{in} = -9$ mm – incoming beam's – and $R_{out} = 11$ mm – outgoing beam's radii of curvature, respectively –, $L = 106$ mm – microfluidic channel width –, $t_m = 170\,\mu$m – coverslip thickness (wall 1 of device), – $t_m = 4$ mm the back reflecting mirror thickness.

4.1.3 Change in the CFL vs. cell size change

The calculations in section (2.4.1) were based on a thin lens formulation of the problem, especially suited to cells whose thickness is smaller than their cross-section. Tetraselmis algae are a good example (cf. algae's image in Fig. (3.9)), but we found the approximation to hold even for more spherical cells. The rate of CFL change for a thin lens, eq. (2.56), as a function of the cell's radius of curvature reads:

$$\frac{\mathrm{d}f_c}{\mathrm{d}r_c} = \frac{1}{2(n_c - n_w)}, \tag{4.1}$$

showing that the change in the cell's focal length (i.e., its derivative) is a constant which only depends on the two refractive indices of water and cell.

Let us examine the situation where the lens thickness has to be taken into account, expressed by:

$$\frac{1}{f_c} = (n_c - n_w)\left(\frac{2}{r_c} - \frac{(n_c - n_w)}{n_c} \cdot \frac{\ell}{r_c^2}\right), \tag{4.2}$$

where ℓ is the cell's diameter, and all other quantities are the same as before. The positions of real and virtual images are measured from the two principal planes H_1 and H_2, in the thick lens expression. Since we consider the cell as a symmetric thick lens, the planes are defined by $H_1 = V_1 - H_c$ and $H_2 = V_2 + H_c$ (cf. Fig. (4.3)) where H_c is defined by:

$$H_c = -f_c \frac{(n_c - n_w)l}{n_c r_c}, \tag{4.3}$$

and V_1, V_2 are the intersections of the thick lens with the optical axis (cf. Fig. (4.3)).

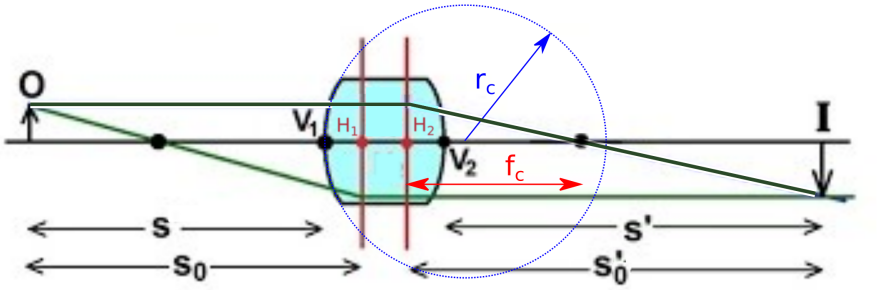

FIGURE 4.3. Schematics of a thick lens: r_c represents the cell's radius of curvature (blue circle), the focal length f_c (red) is measured from the principal plane H_2 is shown in red. V_1 and V_2 are the intersections of the lens with the optical axis, while the green rays are the rays used to create the real image **I** from the object **O**, S and S_0 is the distance between the object and the principal planes while S', and S'_0 are the distances between the real image and the principal planes.

The derivative of the CFL f_c respect the cell radius of curvature r_c that indicates the change of the cell focal length with the radius of curvature in a thick lens representation is:

$$\frac{\mathrm{d}f_c}{\mathrm{d}r_c} = \frac{n_c}{n_c - n_w} \cdot \frac{2r_c}{2r_c n_c - l(n_c - n_w)} \left(1 - \frac{r_c n_c}{2r_c n_c - l(n_c - n_w)}\right). \tag{4.4}$$

$\frac{\mathrm{d}f_c}{\mathrm{d}r_c}$ vs. r_c is plotted in Fig. (4.4).

The parameters $n_w = 1.33$, $n_c = 1.38$ and $l = 30\,\mu$m were held constant, while the cell's radius of curvature was varied from 1 to 30 μm. The situation $r_c << l$ is an extreme case of a thick lens, a cylinder would represent this with polar caps at its endpoints. On the other hand, $r_c >> l$ is the ideal thin lens situation. And between the two extrema, we find the spherical cell, with $r_c = l/2$ ($r_c = 15\,\mu$m in the Fig. (4.4)). Only cells with shape varying between spheres and flattened oval shapes (cf. Fig. (3.9)) can be found in the experiment, since the extreme shape of the cylinder with polar caps – up to $r_c = 6\mu m$ in Fig. (4.4) – would be rotated by the acoustic device and no longer have their curved ends aligned with the resonator axis. This would be the case of elongated cells, like bacteria, which would be aligned with the flow. The "cylindrical" geometry is included in the figure to show the evolution of the focal length.

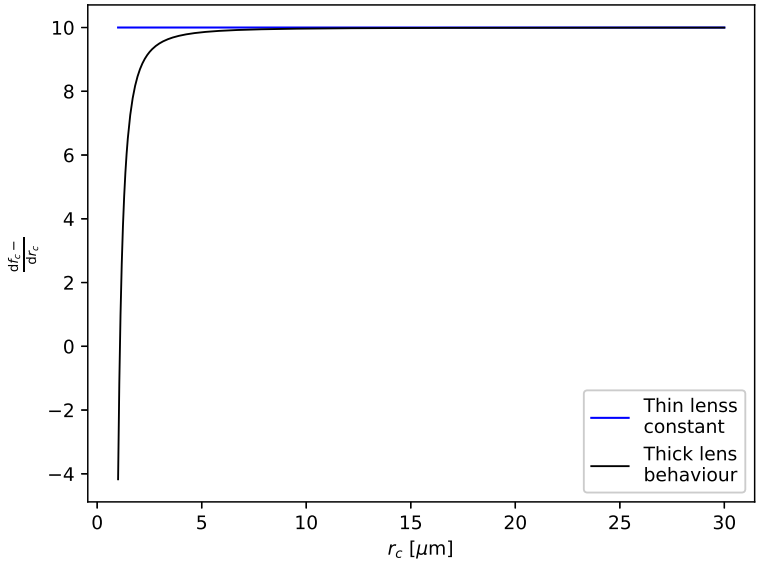

FIGURE 4.4. Comparison of the focal length's, f_c, derivative, relative to the radius of curvature r_c, between thin (blue line) and thick lens (black line). Parameters: cell, $n_c = 1.38$, and water, $n_w = 1.33$, refractive indices, respectively, and cell diameter $l = 30\mu m$.

The comparison between the focal length's derivative with respect to r_c shows that starting from the spherical cell, the thin lens approximation is excellent (near coincidence between blue and black lines). This is due to the small change in refractive index between water and cell, which produces an equivalent focal length much larger than the sphere diameter, thus providing a good thin lens representation even for a physically thick cell. Also, as mentioned above, acoustic focussing ensures that non-spherical cells will be aligned with their larger surface parallel to the channel wall. As an example, we see (Fig. (2.1)) that RBCs are rotated to travel along the channel with their flatter surface facing the walls, thus the incident laser beam (and the resonator axis). This analysis confirms, therefore, the validity of the thin lens approximation for our device.

4.1.4 Defocussing effect

As presented in section 3.1.2, the CFPP measurements were made with a distance of 35 μm between the focal plane and cells' displacement plane or defocussing. This defocusing implies a magnification $\mathfrak{m}$ of the observed fringe pattern. Finesse is invariant under this magnification:

$$\mathscr{F} = \frac{\mathfrak{m} \cdot \mathrm{FSR}}{\mathfrak{m} \cdot \mathrm{FWHM}} = \frac{\mathrm{FSR}}{\mathrm{FWHM}} \tag{4.5}$$

However, the CFL is not invariant under this magnification effect. The equation for the R_{out} (cf. section 2.4.2.1) with the magnification $\mathfrak{m}$ now reads:

$$R_{out} = \pm\sqrt{\frac{1}{4k^2}\left[\mathfrak{m}^2\rho_2^2 - \mathfrak{m}^2\rho_1^2 - k^2\right]^2 - \mathfrak{m}^2\rho_1^2}\,, \tag{4.6}$$

$$k = \lambda + \sqrt{R_{in}^2 + \mathfrak{m}^2\rho_2^2} - \sqrt{R_{in}^2 + \mathfrak{m}^2\rho_1^2}\,, \tag{4.7}$$

where the magnification $\mathfrak{m}$ is determined by [44]:

$$\mathfrak{m} = \frac{f}{d-f} \tag{4.8}$$

f is the objective's focal length, and d is the distance to the object; in this case, the cell. Substituting equation (4.6) in the formulae presented in section (2.4.1.2) to compute the CFL allows for the computation of the magnification effect $\mathfrak{m}$ on the $f_{c,+}$. The results are plotted in Fig. (4.5). From the plot, we can observe that the magnification effect on the CFL is negligible since the significant digits (the integers) remain unchanged. This result matches the calculations shown in section (2.4.2.2) (cf. Fig. (2.20)) from which we concluded that in order to have a significant change in the $f_{c,+}$ the input radius of curvature has to vary a few mm.

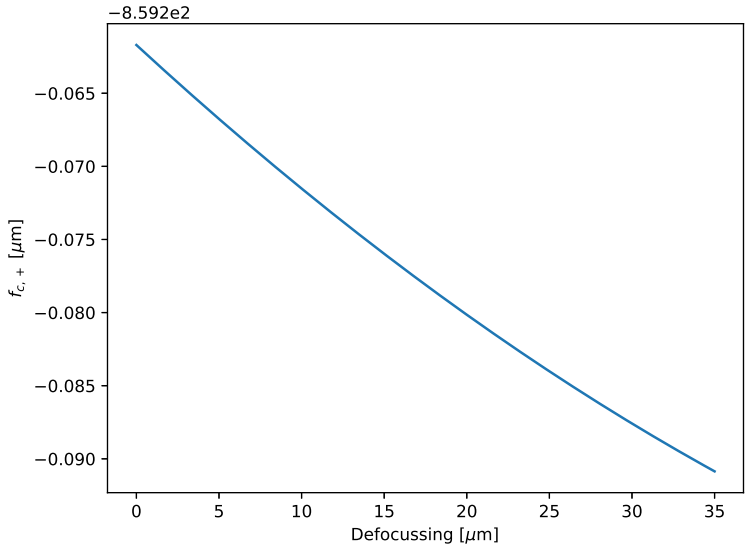

FIGURE 4.5. The figure shows the effect of the magnification on the CFL originated by 35 μm defocussing. The $f_{c,+}$ in the upper corner is -859.2 [μm] from which the y-axis values are added. Mentioned value corresponds to $\rho_1 = 21.7\,\mu$m, $\rho_2 = 46.2\,\mu$m, $R_{in} = -9$mm and $R_{out} = 1.14$ mm.

Thus, the magnification $\mathfrak{m}$ of the interference fringes allows for better resolution, thus more accurate measurements and reliable results. However, the influence of defocussing on the evaluation of the equivalent focal length is negligibly small and non-existent on the evaluation of the Finesse.

4.1.5 Chemical calibration

External control on cell mechanics is of great help in the development and calibration of mechanical cytometry devices, such as AID. Cellular mechanical properties can be dramatically altered using exogenous chemicals that affect components of the cytoskeleton or nucleus. Traditionally, researchers have used these chemicals to modify the architecture of the cytoskeleton, resulting in a modified mechanical phenotype [21]. Approximately half of the approved drugs target human membrane proteins on the cell surface, such as G-protein coupled receptors (GPCRs) [67]. Drugs like dexamethasone and daunorubicin, produce an overall stiffening of whole-cell properties in leukemic cells. Studies of cell mechanics often use exogenous chemicals, such as cytochalasin B and D, latrunculin A, or jasplakinolide, to disrupt the organization of actin filaments, resulting in decreased elasticity. Blebbistatin has been used to inhibit nonmuscle myosin II, preventing active contraction of the cytoskeleton and causing a concurrent softening of the whole-cell [70, 86].

Drugs such as estramustine, colchicine, paclitaxel, eribulin, and discodermolide act by modifying cytoskeletal function, specifically microtubule dynamics, in cells that are actively dividing [59]. Using cell mechanics as a proxy for cytoskeletal changes may also enable screening libraries of drugs to identify those affecting cytoskeleton or nuclear architecture. This screening process would be label-free, requiring no immunolabeling or complex interrogation of cell behavior [21].

4.2 Quasi-real-time implementation

Real-time cytometry based on label-free markers, such as cell mechanics, is a relatively new technique. For instance, the reference technique in the field, the Real-Time Deformability Cytometry (RT-DC), was reported for the first time in 2015 [78] (cf. section (1.6.1)). It enabled the real-time analysis of mechanical properties with more than 100 cells/s.

The AID is potentially capable of operating in real-time when working on its detector-based operation mode. It provides, potentially, much higher resolution and offers the possibility to tune the mechanical stimulus. In fact, the reliance of our technique on a 1D analysis strongly reduces the computational complexity. We have implemented a real-time automatic cell analysis of the time traces acquired with the photodiodes detectors (cf. section (2.1)) to measure the Finesse and FSR of the CFPP. In Fig. (4.6), a time trace containing the CFPP of two different polystyrene beads is shown. The time traces sections corresponding to 0.30 to 0.55 s and 1.30 to 1.50 s in figure Fig. (4.6) are referred to as valleys. Each valley corresponds to the intensity profile of one single fringe pattern perturbation. Below is detailed how the valleys are identified and how the contained CFPP is quantified using a Python script.

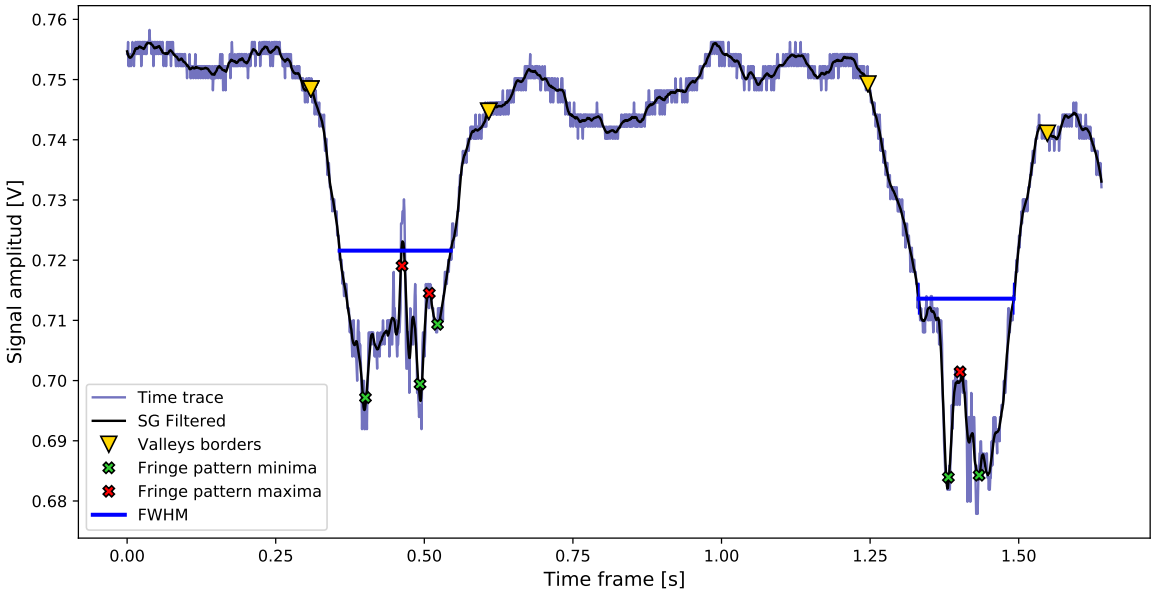

FIGURE 4.6. Two polystyrene 3μm diameter bead time trace. The CFPP computational analysis is done in real-time. The time trace (blue-grey) is smoothed using the Savitzky-Golay filter, the borders of the perturbation (named valley) are identified (yellow arrows) useful to determine the structure's FWHM related to the cell size. Finally, maxima and minima (red and green "x" marks, respectively) inside the valley are identified and measured.

The DSOXJ.py file Python script is written starting from Dr.Sthépahe Barland code's DSOX.py (based on vxi11Device Python library to interface the oscilloscope Keysight DSOX3014A) to acquire the time

traces. In the code, the SGF and the `find_peaks` function (cf. section (3.2.2)) have been implemented to determine the number of valleys present in a time sequence array. Next, the identification of maxima and minima in the fringe pattern profile is carried out. A detailed description of this process is presented in the subsections below, while the Python script and observations on its performance can be found in the appendix.

4.2.1 Finding Valleys

First, the SGF and the `find_peaks` function are used to identify the valleys. This is achieved by identifying the minimum, y_{min}, maximum, y_{max}, and average, y_{av}, values in the y-axis of the time trace. These parameters are used to set the Prominence P_v and the Height value H_v as follows:

$$P_v = \frac{y_{\max} - y_{\min}}{4} \tag{4.9}$$

$$H_v = y_{\text{av}} \tag{4.10}$$

In this way, just the two bumps belonging to the two valleys in Fig. (4.6), will be identified and measured by the `find_peaks` function. It is important to notice that the retrieved FWHM of the valley (blue line in Fig. (4.6)) is directly proportional to the cell's size.

4.2.2 Finding Valleys Borders

Once the valley has been found, it becomes necessary to identify its borders. Borders will mark off the time trace region, which contains information about the CFPP. By taking the second derivative of the time trace by means of the SGF and then inverting it $(1 - f(t))$, the inflection points become peaks while the rest of the data flattens, the red line in Fig. (4.7). The `find_peaks` function is used to identify these inflection points, which are then used as valley borders (yellow triangles the Figs. (4.6) and (4.7)).

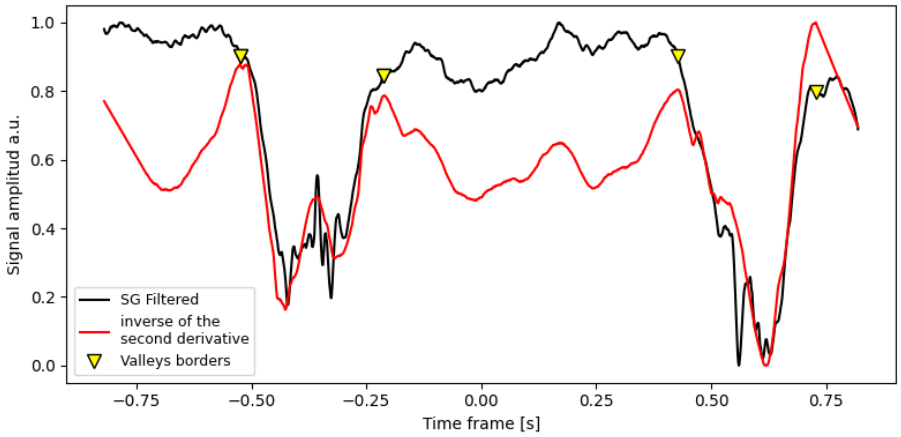

FIGURE 4.7. Valleys borders identification based on the detection of the inflection points of the SG filtered time trace (black line). The Savitzky-Golay filter is used to compute the second derivative of the signal, then the result is inverted $(1 - f(t))$, and the `find_peaks` function is used to identify the peak associated with the inflection points, i.e., the valley borders (yellow triangles).

4.2.3 Measuring the CFPP inside the valleys

Since valley borders allow for the CFPP measurement inside each valley, the time interval they delimit can be separated from the rest for individual analysis. The `find_peaks` function is again used to identify and measure the peaks. Moreover, the vertical scale of the data is different inside the valley. Thus new parameter values need to be computed. The new criteria for the prominence value P_v and the height value H_v are:

$$P_v = \frac{yv_{\max} - yv_{\min}}{10}, \tag{4.11}$$

$$H_v = \frac{yv_{\max} - yv_{\min}}{12}, \tag{4.12}$$

where $yv_{\max}$ and $yv_{\min}$ are the maximum and minimum y-axis value of the time traces inside the borders of the valley for each valley. The new P_v and H_v criteria have been optimized to accurately detect the maxima and minima with respect to the new intervals in the time trace. The peak-baseline ratio is different from the one used to find the valley bottom. The returned values of the `find_peaks` function allow for the CFPP's maxima and minima retrieval (red and green x marks in Fig. (4.6)) and thus for the computation of the corresponding FWHM and FSR for each cell.

4.2.4 Two detectors

The AID is provided with two photodiode detectors (cf. section (2.1.3)). In principle, the time trace analysis presented above can be carried out with a single detector measuring the light intensity changes occurring on the resonator axis, D_1 in Fig. (4.8). However, a second detector D_2 has been introduced to have an accurate measurement of cell speed, which is necessary for determining its size in the y-direction.

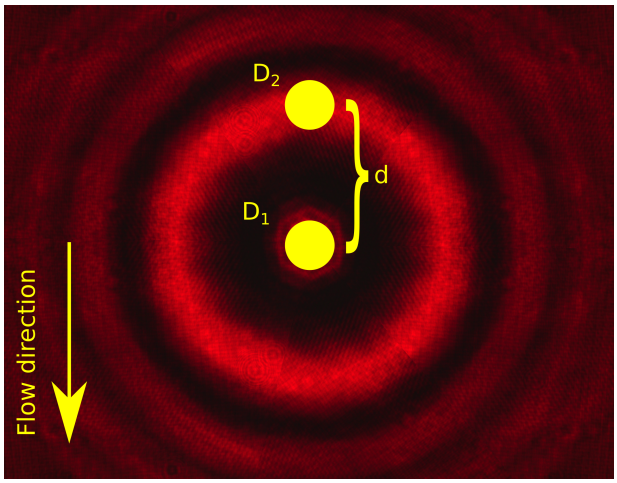

FIGURE 4.8. The resonator fringe pattern devoid of cells is shown. The detection points of the photodiode detectors D_1 and D_2 are marked in yellow, where their separation defines the distance d.

As mentioned above (in section (4.2.1)), the valleys' full width at half maximum FWHM_t (here measured in time) is directly proportional to the cell's size. The cell diameter ℓ and the speed v_c are related as follows:

$$\ell \propto v_c \cdot \mathrm{FWHM}_t \tag{4.13}$$

The cells' velocity can be determined by placing the detection point of detector D_1 on the resonators axis and the detection point of the detector D_2 in a different position along the cells' trajectories. In Fig. (4.8) the second detector D_2 has been placed on the next bright fringe of the RFP aligned with flow direction, thus defining the distance d between the detection points. Next, the time gap t_g between the detectors signal (cf. Fig. (4.9)) can be used to measure the travel time of the cells (cf. Fig. (4.9)) and thus calculate their velocity.

Thus, the introduction of the two diode detectors allows for the implementation of real-time analysis of the CFPP isolated from the time traces valleys and for the real-time measurement of the cell's diameter based on the two detector system. The real-time analysis is made possible by the fact that the detectors' and electronic response time is extremely short compared to the timescales of particle motion.

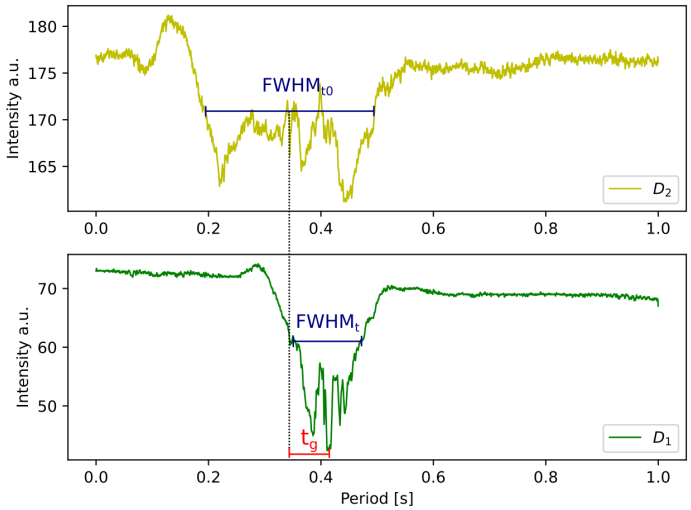

FIGURE 4.9. The time traces acquired with the detectors –in the points marked in Fig. (4.8)– for the same yeast cell. The time gap between the time traces is measured from the center of the valleys (marked in red).

The time traces shown in Fig. (4.9) belong to the same yeast cell flowing inside the microfluidic channel and crossing the detection point as established in Fig. (4.8). Even though the time traces belong to the same cell, they present a different FWHM_t mainly for two reasons: 1) The oblique illumination that the cell receives since the top detector is placed off-axis (i.e., the first signal is taken before the cell reaches the resonator axis); and 2) the different sizes of first fringe and central spot (governed by the angle θ in the phase – argument of the Airy function, see eq. (1.16)) even when the cell is placed on-axis . Thus, the FWHM_t value that should be used to measure the cell diameter ℓ is measured on the time trace coming from the D_1 detector.

4.3 Potential applications

One of the primary applications of cell mechanical phenotyping is the characterization cell modifications. Whether as a means for better understanding a disease or simply as a diagnostic approach, testing the mechanical properties of single cells can provide clear indications of dysfunction. The biophysical properties of cells, such as their compressibility, are closely related to disease progression, for instance in cancer development and metastasis [110]. Besides, cell mechanics plays a fundamental role in the human immune system, which is well-illustrated by leukocyte extravasation [29]. Thus, we envisage medical diagnostic applications for AIT, together with cell sorting and drug screening. Its potentially very low cost renders it suitable for economically vulnerable populations.

4.3.1 Cancer

Cancer is a prominent target of investigation for which AIC can serve as a powerful tool. Researchers have repeatedly observed that malignant cells exhibit a more compliant phenotype than their healthy counterparts, presumably because compliance provides an advantage for invading surrounding tissues. More specifically, as cells become malignant, mechanical changes have been attributed to an increasingly disorganized cytoskeleton and less pronounced cortical actin [98, 73]. In most cases oncogenic transformation leads to larger deformability of single cells, as it has been reported for various cancers, such as bladder, prostate, thyroid and ovarian ones [65].

One of the most highly metastatic types of cancer is melanoma, which has a very unusual property: it can synthesize the pigment melanin in large amounts, becoming heavily pigmented. Melanin in pigmented cells, including melanoma cells, is in the form of granule-like organelles called melanosomes. These organelles were recently found to have unusual mechanical properties, being very stiff and hard to deform. Cells with a high concentration of melanin can be up to 10 times stiffer than non-pigmented cells [89]. Noticeably, the incidence rate of melanoma in the white race is 20 times higher than in the black race. The risk of suffering melanoma during lifetime is 2.6 % for White people, 0.1 % for Black people and 0.6 % for Hispanic people [87].

On the other hand, increased tissue stiffness is a classic characteristic of solid tumors [80]. One of the major contributing factors is the increased density of collagen fibers in the Extracellular Matrix (ECM). Studies of how cancer cells biomechanically interact with and respond to the stiffness of the ECM [113] have shown that only malignant cancer cells have the ability to adjust to collagen matrices of different densities. Employing microrheology on the biologically relevant spheroid invasion assay, it was shown that, even within a cluster of cells of similar origin there are differences in the intracellular biomechanical properties depending on the cells' invasive behavior. For instance, an increase in viscosity is observed in cancer cells that facilitate their invasion into the collagen matrices. The hypothesis is that differential viscoelasticity might facilitate spheroid tip invasion through a dense matrix. These findings highlight the importance of the biomechanical interplay between cells and their microenvironment for tumor progression.

Architectural features of cells have long been recognized as useful for identifying and staging malignancy. Analyzing these features in cells from body fluids and biopsies has become a routine test in cytology and pathology labs. Some cancer cells can be up to 32 times more elastically compliant than their healthy

counterparts [65]. Features of the cytoplasm and, in particular, nuclear architecture such as chromatin condensation, nuclear envelope shape, metaphase nuclei, and the nuclear-cytoplasmic ratio are used to arrive at a diagnosis of potential malignancy, which is important to direct subsequent clinical care for the patient [71].

A quantitative example can be found in the investigation of Guck et al. [41] investigated BALB/3T3 and SV-T2 fibroblasts with the microfluidic optical stretcher. BALB/3T3 is a fibroblast cell line established in 1968 from disaggregated BALB/c mouse embryos. SV-T2 cells are derived from BALB/3T3 cells by transformation with the oncogenic DNA virus SV40. Measuring large numbers of cells reveals that the optical deformability of malignantly transformed SV-T2 fibroblasts is significantly shifted to higher values compared to normal BALB/3T3 fibroblasts: $\mathrm{OD}_{\mathrm{BALB/3T3}} = 8.4 \pm 1.0$, $\mathrm{OD}_{\mathrm{SV-T2}} = 11.7 \pm 1.1$ – cf. Fig. (4.10).

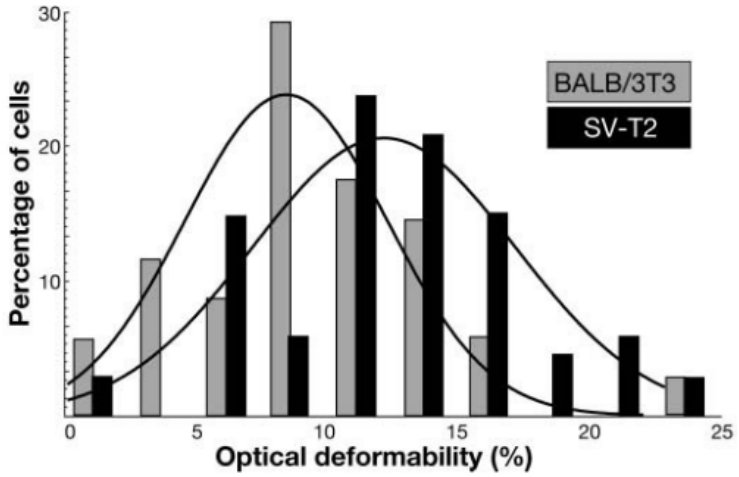

FIGURE 4.10. Malignant fibroblast cells SV-T2 are more elastically compliant than the healthy fibroblast BALB/3T3. Taken from [41].

High-throughput approaches to mechanical phenotyping such as ours – also sensitive to cellular architecture – are ideal for making an impact in the cytopathology lab through the quantitative and automated diagnosis of these samples. Thus, the AID contributes to satisfying the need, established in [21], to apply new technologies to improve sensitivity, reduce processing time and cost, and provide quantitative and comparable test results.

4.3.2 Parasites and liquid tumors

The blood cell deformability is a critical aspect, and assessing the cell deformation characteristics is essential for better diagnostics of healthy and deteriorating blood cells, like in the case of sickle or malaria for (RBC) or leishmaniasis in the case of white blood cell (WBC) [35]. By using AFM in a 2×2 mm area in the central region of the RBC. Young's moduli were extracted using a Hertz fit, see Fig. (4.11). That area was chosen since is where the height reaches maximum values (>2-3 μm). hRBCs have a mean Young's modulus value of (29 ± 6) kPa, while spherocytotic RBCs are stiffer at (101 ± 9) kPa [29]. These values, in combination with the AIT, would serve as a powerful diagnostic tool.

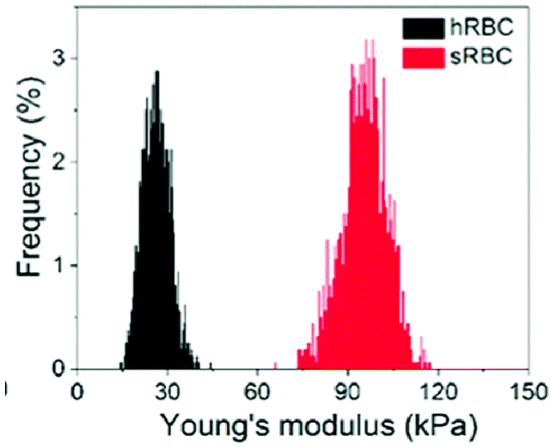

FIGURE 4.11. Histograms showing the mechanical properties of healthy RBCs (hRBCs) and sRBCs as measured by FD-based AFM. A 3-fold increase in Young's modulus is observed on hereditary spherocytosis RBC (sRBCs) as compared to hRBCs. The data were acquired at an oscillation frequency of 0.25 kHz and are representative of 3 healthy donors and 3 patients with HS. A total of 27 cells for each condition were analyzed during 6 independent experiments. Taken from [29].

Malaria is one disease that has been extensively studied for its effects on the mechanical properties of cells. When RBCs are infected with the parasite *Plasmodium falciparum* (Pf), they lose their deformability. The intraerythrocytic development of Pf parasites includes three major stages, called ring (0-24 h), trophozoite (24-36 h), and schizont (40-48 h). During this development, the RBC membrane can stiffen by up to a factor of ten in comparison with healthy RBCs [23]. This mechanical change increases the risk of occlusions in the spleen and peripheral capillaries, lowering oxygen concentrations in downstream tissues and eventually leading to necrosis [33]. RBC deformability is also affected in diseases such as sickle cell, sepsis, and diabetes [61]. A fast test for these diseases would be possible by application the AID.

A change in the mechanical properties of elasticity and viscosity also occurs in leukemia. A decreased cell stiffness enhances leukemia development and progression [49]. It has been reported that HL60, Jurkat (human lymphoblast peripheral blood), and neutrophil cells have an apparent stiffness of (855 ± 667) Pa, (48 ± 35) Pa, and (156 ± 87) Pa, see Fig. (4.12). Effect of cell type on stiffness is significant(α = 0.05, p<0.001) when using a one-way ANOVA analysis [84]. For leukemia, a medical diagnosis and drug screening use of the AIT can be expected.

4.3.3 Aging

The aging process, although not a disease, also induces changes in the mechanical properties of individual cells, which may contribute, in part, to the degradation of cellular function. For most cell types, age causes an increase in cell stiffness along with an inability to fully recover large deformations [96] thus aging process could be analyzed with the AIT.

Osteoarthritis is another representative disease that changes the mechanical phenotype of affected cells and typical of aging. Chondrocytes in articular cartilage exhibit a less compliant mechanical phenotype in

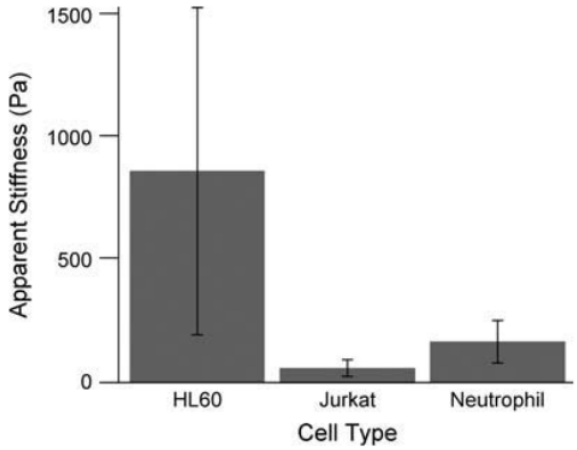

FIGURE 4.12. Comparison of myeloid and lymphoid cell line and neutrophilstiffness at low piezo extension rates. With a piezo rate of 415 nm/s, HL60 cells have an average apparent stiffness of 855 Pa with a standard deviation of 670 Pa (n=60). In contrast, Jurkat cells are significantly softer ($p < 0.001$), with an average apparent stiffness of 48 Pa and a standard deviation of 35 Pa (n=37). Neutrophils have an average apparent stiffness of (156±87) Pa (n=26, mean±SD), significantly softer than HL60 cells and significantly stiffer than Jurkat cells ($p<0.001$ for both). Taken from [84]

diseased tissue compared with healthy tissue, which is likely induced as a compensatory mechanism for the higher strains existing in the degraded cartilage [101]. The AID can be used to measure and quantify the aging effect on cells.

4.3.4 Mechanotransduction

Mechanotransduction is the process through which cells sense and respond to their mechanical environment. During mechanotransduction, mechanical signals are sensed and activate intracellular biochemical signaling pathways. Cells sense the mechanical properties of their environment and use the information that they acquire to inform gene expression and cell fate decisions [53]. The AID cell optomechanical properties assessment can be used to research cell mechanotransduction processes such the following.

Cells exert forces against their environment through dynamic cytoskeletal remodeling. Mechanical forces are critical to modulate cell spreading, contractility, gene expression, and even stem cell differentiation [30]. In most cases, it is the filamentous actin (F-actin) cytoskeleton that bears most of the mechanical load. The force exertion is the contraction of antiparallel actin filaments by the myosin II motor. Myosin II based pulling was initially characterized as the mediator of muscle contraction; it is now clear that it drives shape change in most eukaryotic cells. Protrusive F-actin based structures can deform underlying substrates as well as the surfaces of other cells, and this implies that they are capable of transmitting forces [53]. The nucleus is critical in mechanosensing, as it transmits external forces from the cellular microenvironment to the nuclear envelope housing chromatin, leading to genetic changes in the cell [17, 24, 53, 64].

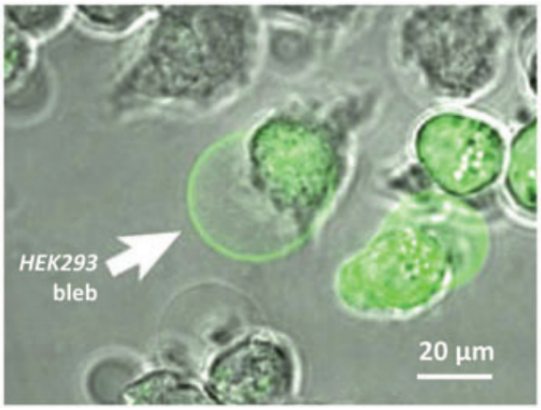

FIGURE 4.13. PIEZO1-GFP expression in HEK293 blebs. The diameters of the blebs reach 15 mm. Mechanical activation of PIEZO1-GFP in bleb-attached patches with a pressure pulse of 55 mmHg. Pipette potential was held at 75 mV. Taken from [17].

Mechanosensitive ion channels are force-transducing molecules that couple mechanical stimuli to ion flux. Understanding the gating mechanism of mechanosensitive channels is challenging because the stimulus seen by the channel reflects forces shared between the membrane, cytoskeleton and extracellular matrix. By generating HEK293 cell membrane blebs largely free of the cytoskeleton and using the bacterial channel Large Conductance Mechanosensitive Ion Channel (MscL), a calibration of the bilayer tension was performed, demonstrating that activation of MscL in blebs is identical to that in reconstituted bilayers. Utilizing a PIEZO1-GFP fusion is shown that PIEZO1 is activated by bilayer tension in bleb membranes, based on the fluoresce observation taking place after the bleb is mechanically stimulate, see Fig. (4.13) [16].

4.3.5 Analysis of Immune Status

When lymphocytes are activated, e.g., as a result of infection with the Epstein-Barr virus, gross changes occur in nuclear condensation, and cell size, the high sensitivity of the AID is potentially applicable to detect such changes (hence the infections) in early stages. Measurements of deformability, using the AID, may be used diagnostically to quickly identify or rule out viral infections that lead to large quantities of circulating reactive or activated lymphocytes [21].

4.3.6 Drug screening

Nowadays, it is becoming more common to find antibiotic-resistant infections. Thus the need to finding new drugs with higher specificity and to speeding up the screening process to shorten as much as possible the drug discovery phase of these new drugs is highly desirable. Our AIT may be suited to this task, especially when the biomarker is bacteria elasticity, as in the following examples.

Research has shown that bacterial resistance to antibiotics is encoded in genetic mechanisms, impacting their mechanical properties. For instance, the elasticity of cells exposed to ampicillin for 3 h were slightly more heterogeneous than cells exposed to ampicillin for 8 h or than cells of the control. Such change in

elasticity is related to the production of hydrolyzing enzymes involved in the hydrolysis of the β-lactam ring, modification of the target sites to antibiotics such as changes in the penicillin-binding protein resulting in decreased affinity to β-lactams, production of efflux pumps on the cell membrane to expel antibiotics outside the cell, and production of key extracellular polymeric substances that affect the formation of biofilms capable of impeding the diffusion of antibiotics into biofilms [104].

The cell envelope's mechanical properties in Escherichia coli, the lipoprotein Lpp provides the only covalent crosslink between the outer membrane and the peptidoglycan. Mathelié-Guinlet et al. [72] use single-cell atomic force microscopy and genetically engineered strains to study the contribution of Lpp to cell envelope mechanics. They show that Lpp contributes to cell envelope stiffness in two ways: by covalently connecting the outer membrane to the peptidoglycan and by controlling the width of the periplasmic space. Furthermore, mutations affecting Lpp function substantially increase bacterial susceptibility to the antibiotic vancomycin, indicating that Lpp-dependent effects can affect antibacterial drug efficacy.

4.3.7 Device bulk construction and miniaturization

The AIT diagnosis potential will be leveraged if possible to apply this technology with a low operative and low production cost. Thus, it is our intention to turn it into an inexpensive and portable diagnosis device to target the diseases mentioned above. A device like this would have a favorable impact on the health care quality of low-income or hard-to access-regions in the world.

The integration of the microfluidic channel, together with the piezoelectric transducer and the optical cavity shown in Fig. (2.1) the focus lens and diode laser can be built into one single unit made out, for instance, with a polymeric plastic (like Polydimethylsiloxane (PDMS)). This experimental configuration will provide an inexpensive, compact prototype easy to transport and low-cost to build.

4.3.8 Cell sorting

Finally, we present the AIT potential usefulness in cell sorting. In general, the diagnostic applications of a mechanical biomarker rely solely on measuring the mechanical properties of a cell; however, potential therapeutic applications or downstream molecular diagnostics could benefit from mechanics-based approaches to separation. AIT possesses cell sorting potential since it could combine microfluidic cytometry with some other technique to perform the cells' sorting task, for instance, using machine learning [68, 108] or acoustic tweezers [25]. Sorting platform based on real-time fluorescence and deformability cytometry (RT-FDC), is capable of sorting cells based on their defrormability. A standing surface acoustic wave (SSAW) and artificial intelligence are use in the Sorting RT-FDC (soRT-FDC) to effectively sort cells (cf. Fig. (4.14)).

Just as fluorescence-activated cell sorting FACS enabled identifying molecular signatures accompanying subsets of leukocytes based on their immunophenotypes sorting based on mechanophenotypes could provide a unique understanding of the molecular underpinnings of cell mechanics. Such tools could enable new insights into which genes are responsible for controlling cellular architecture, and in heterogeneous populations of diseased cells, help isolate genetic mutations or epigenetic changes underlying uniquely stiff or compliant phenotypes. The cell's sorting AIT-based can potentially reproduce these results in a label-free way, thus eliminating the restriction that fluorescent dyes imply.

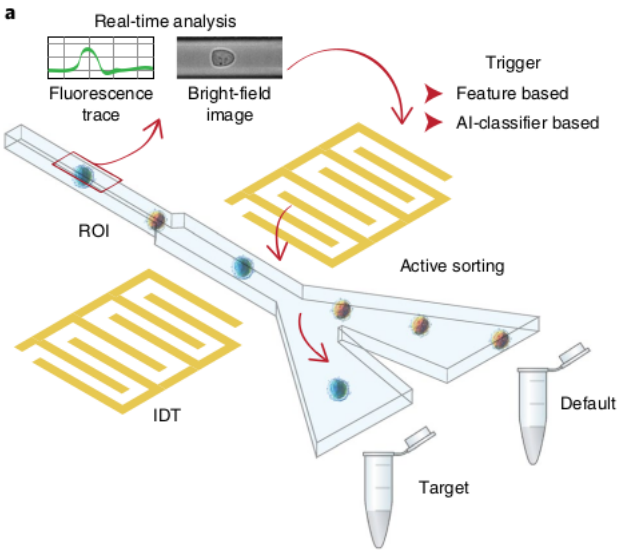

FIGURE 4.14. Operation principle of a soRT-FDC device. Flowed-in cells are deformed in a constriction of the microfluidic channel and analyzed in the region of interest (ROI, outlined in red) in real-time. The SSAW deflects selected cells to the target outlet. AI indicates artificial intelligence. Taken from [77].

In blood, the separation of diseased RBCs or pathologically activated white blood cells (WBCs) may have therapeutic benefits. Using mechanics as a label-free biomarker has intrinsic advantages for such an application, in which unadulterated, healthy blood cells are reintroduced to a patient. Such a dialysis-like therapeutic [60] could potentially be applied to remove more deformable, activated immune cells to reduce organ failure in sepsis patients, malignant bone marrow cells for autologous transplantation of the remaining nonmalignant cells, stiffer malaria-infected cells, or sickled RBCs during a sickle-cell crisis [21]. The 1D cell analysis of the AID would be ideal for blood separation-based treatment. It provides a quasi-real-time analysis of the cells, thus enabling the cells sorting and the reintroduction of the selected cell to the patient.

4.4 Chapter summary

The AID features are discussed in light their optimization (cf. section (4.1)). The back mirror reduces the device's sensitivity, while the resulting ideal configuration is obtained with a planar mirror. The channel width does not strongly influence the measurement quality. Thus it is preferable to increase its value to permit operation at lower frequencies since it enables the use of conventional, less expensive electronics.

The analysis of the out-of-focal-plane image collection, implemented in section (3.1.2), is shown to improve the definition of CFPP. In section (4.1) we analyze its impact on the measurement of CFL and Finesse, showing that it is practically non-existent for the latter and negligible for the former.

One of the main appealing features of the AID, in addition to the contactless, global deformation and non-invasive measurement, is its high throughput and real-time assessment of the optomechanical properties of cells. The first steps towards that end are presented in section (4.2). A python script is

presented to identify and measure the CFPP contained in the time traces acquired with the AID's optical detectors.

Cell mechanical phenotyping can be used to characterize cell modifications. Testing the mechanical properties of single cells can provide clear indications of dysfunction, whether as a tool for better understanding a disease or simply as a diagnostic approach. The biophysical properties of cells, such as their compressibility, have been closely related to disease progression, i.e., cancer development and metastasis. An additional potential biomarker easily detected by the AID is the change in cell refractive index. Finally, some potential applications in the research and diagnosis of the AID are presented in section (4.3). Such applications include; research and diagnosis of cancer, parasites and liquid tumors; mechanotransduction-based treatments; cell aging research; analysis of the immune status; drug screening and cell sorting.

BIBLIOGRAPHY

[1] R. ARMSTRONG, *An introduction to analysis of variance (anova) with special reference to data from clinical experiments in optometry*, Ophthalmic and Physiological Optics, 20 (2000), pp. 235–241.

[2] A. ASHKIN, *Acceleration and trapping of particles by radiation pressure*, Physical Review Letters, 24 (1970), pp. 156–159.

[3] A. ASHKIN, *This contribution is part of the special series of inaugural articles by members of the optical trapping and manipulation of neutral particles using lasers*, Physics National Academy of Sciences, 94 (1997), pp. 4853–4860.

[4] E. U. AZELOGLU, J. BHATTACHARYA, AND K. D. COSTA, *Atomic force microscope elastography reveals phenotypic differences in alveolar cell stiffness*, Journal of Applied Physiology, 105 (2008), pp. 652–661.

[5] W. D. BACHALO, *Method for measuring the size and velocity of spheres by dual-beam light-scatter interferometry*, Applied Optics, 19 (1980), p. 363.

[6] N. BAO, G. C. KODIPPILI, K. M. GIGER, V. M. FOWLER, P. S. LOW, AND C. LU, *Single-cell electrical lysis of erythrocytes detects deficiencies in the cytoskeletal protein network*, Lab on a Chip, 11 (2011), pp. 3053–3056.

[7] D. BHARTI, G. R. SAHOO, S. SHUKLA, AND A. PRADHAN, *Wavelet transform of fourier domain low coherence interference spectra for breast cancer detection*, Tissue Optics and Photonics, (2020).

[8] C. A. BONEAU, *The effects of violations of assumptions underlying the t test.*, Psychological Bulletin, 57 (1960), pp. 49–64.

[9] M. BORN AND E. WOLF, *Chapter x - interference and diffraction with partially coherent light*, in Principles of Optics (Sixth Edition), M. BORN and E. WOLF, eds., Pergamon, sixth edition ed., 1980, pp. 491 – 555.

[10] M. BORN, E. WOLF, A. B. BHATIA, P. C. CLEMMOW, D. GABOR, A. R. STOKES, A. M. TAYLOR, P. A. WAYMAN, AND W. L. WILCOCK, *Principles of Optics: Electromagnetic Theory of Propagation, Interference and Diffraction of Light*, Cambridge University Press, 7 ed., 1999.

[11] R. W. BOYD, *Intuitive explanation of the phase anomaly of focused light beams*, J. Opt. Soc. Am., 70 (1980), pp. 877–880.

[12] S. BYUN, S. SON, D. AMODEI, N. CERMAK, J. SHAW, J. H. KANG, V. C. HECHT, M. M. WINSLOW, T. JACKS, P. MALLICK, AND S. R. MANALIS, *Characterizing deformability and surface friction of cancer cells*, Proceedings of the National Academy of Sciences, 110 (2013), pp. 7580–7585.

[13] J. CASANUEVA DIAZ, *Fabry-perot cavities in advanced virgo*, Control of the Gravitational Wave Interferometric Detector Advanced Virgo, (2018), pp. 37–83.

[14] K. CHALUT, M. HÖPFLER, F. LAUTENSCHLÄGER, L. BOYDE, C. CHAN, A. EKPENYONG, A. MARTINEZ-ARIAS, AND J. GUCK, *Chromatin decondensation and nuclear softening accompany nanog downregulation in embryonic stem cells*, Biophysical Journal, 103 (2012), pp. 2060–2070.

[15] Y.-C. CHEN, Q. CHEN, X. WU, X. TAN, J. WANG, AND X. FAN, *A robust tissue laser platform for analysis of formalin-fixed paraffin-embedded biopsies*, Lab on a Chip, 18 (2018), pp. 1057–1065.

[16] C. D. COX, C. BAE, L. ZIEGLER, S. HARTLEY, V. NIKOLOVA-KRSTEVSKI, P. R. ROHDE, C.-A. NG, F. SACHS, P. A. GOTTLIEB, AND B. MARTINAC, *Removal of the mechanoprotective influence of the cytoskeleton reveals PIEZO1 is gated by bilayer tension*, Nature Communications, 7 (2016).

[17] C. G. CRANFIELD, A. KLODA, Y. A. NIKOLAEV, A. D. MARTINAC, P. RIDONE, N. BAVI, O. BAVI, E. PETROV, A. R. BATTLE, T. NOMURA, P. R. ROHDE, Y. NAKAYAMA, K. R. ROSHOLM, C. D. COX, M. A. BAKER, AND B. MARTINAC, *Mechanosensitivity of ion channels*, Encyclopedia of Biophysics, (2018), pp. 1–11.

[18] F. H. C. CRICK AND A. F. W. HUGHES, *The physical properties of cytoplasm: A study by means of the magnetic particle method part i. experimental*, Experimental Cell Research, 1 (1950), pp. 37–80.

[19] E. DARLING, S. ZAUSCHER, AND F. GUILAK, *Viscoelastic properties of zonal articular chondrocytes measured by atomic force microscopy*, Osteoarthritis and Cartilage, 14 (2006), pp. 571–579.

[20] E. M. DARLING, *Force scanning: a rapid, high-resolution approach for spatial mechanical property mapping*, Nanotechnology, 22 (2011), p. 175707.

[21] E. M. DARLING AND D. D. CARLO, *High-Throughput assessment of Cellular Mechanical Properties*, Annu. Rev. Biomed. Eng, 17 (2015), pp. 35–62.

[22] E. M. DARLING, M. TOPEL, S. ZAUSCHER, T. P. VAIL, AND F. GUILAK, *Viscoelastic properties of human mesenchymally-derived stem cells and primary osteoblasts, chondrocytes, and adipocytes*, Journal of Biomechanics, 41 (2008), pp. 454–464.

[23] A. K. DASANNA, U. S. SCHWARZ, G. GOMPPER, AND D. A. FEDOSOV, *Multiscale modeling of malaria-infected red blood cells*, Handbook of Materials Modeling, (2018), pp. 1–24.

[24] M. T. DOOLIN, T. S. ORNSTEIN, AND K. M. STROKA, *Nuclear deformation in response to mechanical confinement is cell type dependent*, Cells, 8 (2019).

[25] B. W. DRINKWATER, *A perspective on acoustical tweezers-devices, forces, and biomedical applications*, Applied Physics Letters, 117 (2020), p. 180501.

[26] E. DU, Y. QIANG, AND J. LIU, *Erythrocyte membrane failure by electromechanical stress*, Applied Sciences (Basel, Switzerland), 8 (2018).

[27] D.-W. DUAN, Y.-J. RAO, Y.-S. HOU, AND T. ZHU, *Microbubble based fiber-optic Fabry-Perot interferometer formed by fusion splicing single-mode fibers for strain measurement*, Applied Optics, 51 (2012), pp. 1033–1036.

[28] J. S. DUDANI, D. R. GOSSETT, H. T. K. TSE, AND D. D. CARLO, *Pinched-flow hydrodynamic stretching of single-cells*, Lab on a Chip, 13 (2013), pp. 3728–3734.

[29] A. C. DUMITRU, M. A. PONCIN, L. CONRARD, Y. F. DUFRÊNE, D. TYTECA, AND D. ALSTEENS, *Nanoscale membrane architecture of healthy and pathological red blood cells*, Nanoscale Horizons, 3 (2018), pp. 293–304.

[30] Z. FAN, Y. SUN, N. DI CHEN, D. TAY, W. CHEN, C. X. DENG, AND J. FU, *Acoustic tweezing cytometry for live-cell subcellular modulation of intracellular cytoskeleton contractility*, Scientific Reports, 3 (2013), p. 2176.

[31] W. M. FARMER, *Measurement of particle size, number density, and velocity using a laser interferometer*, Applied Optics, 11 (1972), pp. 2603–2612.

[32] M. FAVRE, J. POLESEL-MARIS, T. OVERSTOLZ, P. NIEDERMANN, S. DASEN, G. GRUENER, R. ISCHER, P. VETTIGER, M. LILEY, H. HEINZELMANN, AND A. MEISTER, *Parallel AFM imaging and force spectroscopy using two-dimensional probe arrays for applications in cell biology*, Journal of Molecular Recognition, 24 (2011), pp. 446–452.

[33] D. A. FEDOSOV, H. LEI, B. CASWELL, S. SURESH, AND G. E. KARNIADAKIS, *Multiscale modeling of red blood cell mechanics and blood flow in malaria*, PLoS Computational Biology, 7 (2011), p. e1002270.

[34] M. C. GATHER AND S. H. YUN, *Single-cell biological lasers*, Nature Photonics, 5 (2011), pp. 406–410.

[35] N. M. GEEKIYANAGE, E. SAURET, S. C. SAHA, R. L. FLOWER, AND Y. T. GU, *Deformation behaviour of stomatocyte, discocyte and echinocyte red blood cell morphologies during optical tweezers stretching*, Biomechanics and Modeling in Mechanobiology, (2020).

[36] S. GIRARDO, N. TRÄBER, K. WAGNER, G. COJOC, C. HEROLD, R. GOSWAMI, R. SCHLÜβLER, S. ABUHATTUM, A. TAUBENBERGER, F. REICHEL, D. MOKBEL, M. HERBIG, M. SCHÜRMANN, P. MÜLLER, T. HEIDA, A. JACOBI, E. ULBRICHT, J. THIELE, C. WERNER, AND J. GUCK, *Standardized microgel beads as elastic cell mechanical probes*, J. Mater. Chem. B, 6 (2018), pp. 6245–6261.

[37] P. GLYNNE-JONES, R. J. BOLTRYK, AND M. HILL, *Acoustofluidics 9: Modelling and applications of planar resonant devices for acoustic particle manipulation*, Lab on a Chip, 12 (2012), pp. 1417–1426.

[38] P. GLYNNE-JONES, C. E. M. DÉMORÉ, C. YE, Y. QIU, S. COCHRAN, AND M. HILL, *Array-controlled ultrasonic manipulation of particles in planar acoustic resonator*, IEEE transactions on ultrasonics, ferroelectrics, and frequency control, 59 (2012), pp. 1258–1266.

[39] R. A. GROENEVELD AND G. MEEDEN, *Measuring skewness and kurtosis*, The Statistician, 33 (1984), p. 391.

[40] J. GUCK, R. ANANTHAKRISHNAN, H. MAHMOOD, C. MOON, C. TESS J. ABD CUNNINGHAM, AND J. KAS, *The optical stretcher: A novel laser tool to micromanipulate cells*, Biophysical Journal, 81 (2001), pp. 767–784.

[41] J. GUCK, S. SCHINKINGER, B. LINCOLN, F. WOTTAWAH, S. EBERT, M. ROMEYKE, D. LENZ, H. M. ERICKSON, R. ANANTHAKRISHNAN, D. MITCHELL, J. KÄS, S. ULVICK, AND C. BILBY, *Optical deformability as an inherent cell marker for testing malignant transformation and metastatic competence*, Biophysical Journal, 88 (2005), pp. 3689–3698.

[42] E. GUZNICZAK, M. MOHAMMAD-ZADEH, F. DEMPSEY, M. JIMENEZ, H. BOCK, G. WHYTE, N. WILLOUGHBY, AND H. BRIDLE, *High-throughput assessment of mechanical properties of stem cell derived red blood cells, toward cellular downstream processing*, Scientific Reports, 7 (2017), p. 14457.

[43] D. HARTONO, Y. LIU, P. L. TAN, X. Y. S. THEN, L.-Y. L. YUNG, AND K.-M. LIM, *On-chip measurements of cell compressibility via acoustic radiation*, Lab on a Chip, 11 (2011), pp. 4072–4080.

[44] E. HECHT, *Optics*, Addison Wesley, 2nd ed ed., 1987.

[45] R. HOCHMUTH, N. MOHANDAS, AND P. BLACKSHEAR, *Measurement of the elastic modulus for red cell membrane using a fluid mechanical technique*, Biophysical Journal, 13 (1973), pp. 747–762.

[46] P. HOSSEINI, D. JIN, Z. YAQOOB, AND P. T. C. SO, *Single-shot dual-wavelength interferometric microscopy*, Methods, 136 (2018), pp. 35–39.

[47] V. A. HOSSEINZADEH, C. BRUGNARA, AND R. G. HOLT, *Shape oscillations of single blood drops: applications to human blood and sickle cell disease*, Scientific Reports, 8 (2018).

[48] D. HOU, J. KANG, L. WANG, Q. ZHANG, Y. ZHAO, AND C. ZHAO, *Bare fiber adapter based Fabry-Pérot interferometer for microfluidic velocity measurement*, Optical Fiber Technology, 50 (2019), pp. 71–75.

[49] L. HU, F. NI, X. WANG, M. E. FAY, K. M. YOUNG, W. A. LAM, T. A. SULCHEK, AND C.-K. QU, *Decreased cell stiffness enhances leukemia development and progression*, Leukemia, (2020).

[50] J. HUANG, F. LIN, AND C. XIONG, *Mechanical characterization of single cells based on microfluidic techniques*, TrAC Trends in Analytical Chemistry, 117 (2019), pp. 47–57.

[51] F. T. HUNTER, *A photoelectric method for the quantitative determination of erythrocyte fragility*, Journal of Clinical Investigation, 19 (1940), pp. 691–694.

[52] S. C. HUR, N. K. HENDERSON-MACLENNAN, E. R. B. MCCABE, AND D. DI CARLO, *Deformability-based cell classification and enrichment using inertial microfluidics*, Lab on a Chip, 11 (2011), pp. 912–920.

[53] M. HUSE, *Mechanical forces in the immune system*, Nature Reviews Immunology, 17 (2017), pp. 679–690.

[54] C. IONESCU-ZANETTI, L.-P. WANG, D. DI CARLO, P. HUNG, A. DI BLAS, R. HUGHEY, AND L. P. LEE, *Alkaline hemolysis fragility is dependent on cell shape: Results from a morphology tracker*, Cytometry Part A, 65A (2005), pp. 116–123.

[55] P. ISERMANN AND J. LAMMERDING, *Nuclear mechanics and mechanotransduction in health and disease.*, Current biology, 23 (2013), pp. R1113–21.

[56] M. JANIK, M. KOBA, A. CELEBAŃSKA, W. J. BOCK, AND M. ŚMIETANA, *Live E. coli bacteria label-free sensing using a microcavity in-line Mach-Zehnder interferometer*, Scientific Reports, 8 (2018), pp. 1–8.

[57] P. A. JANMEY AND C. A. MCCULLOCH, *Cell mechanics: integrating cell responses to mechanical stimuli*, Annu. Rev. Biomed. Eng., 9 (2007), pp. 1–34.

[58] N. JIANG, M. YOU, Y. WANG, Y. HUANG, S. XIE, Y. LIN, AND H. YANG, *Probing the biophysical properties of tumor cells during mitosis by atomic force microscopy*, Biomechanics and Modeling in Mechanobiology, 17 (2018), pp. 1209–1215.

[59] M. A. JORDAN AND L. WILSON, *Microtubules and actin filaments: dynamic targets for cancer chemotherapy*, Current Opinion in Cell Biology, 10 (1998), pp. 123–130.

[60] J. H. KANG, M. SUPER, C. W. YUNG, R. M. COOPER, K. DOMANSKY, A. R. GRAVELINE, T. MAMMOTO, J. B. BERTHET, H. TOBIN, M. J. CARTWRIGHT, A. L. WATTERS, M. ROTTMAN, A. WATERHOUSE, A. MAMMOTO, N. GAMINI, M. J. RODAS, A. KOLE, A. JIANG, T. M. VALENTIN, A. DIAZ, K. TAKAHASHI, AND D. E. INGBER, *An extracorporeal blood-cleansing device for sepsis therapy*, Nature Medicine, 20 (2014), p. 1211,Äì1216.

[61] L. A. KIRSCHENBAUM, M. AZIZ, M. ASTIZ, D. SAHA, AND E. RACKOW, *Influence of rheologic changes and platelet-neutrophil interactions on cell filtration in sepsis*, American Journal of Respiratory and Critical Care Medicine, 161 (2000), pp. 1602–1607.

[62] N. R. LABRIOLA AND E. M. DARLING, *Temporal heterogeneity in single-cell gene expression and mechanical properties during adipogenic differentiation*, Journal of Biomechanics, 48 (2015), pp. 1058–1066.

[63] E. N. LAZAREVA AND V. V. TUCHIN, *Blood refractive index modelling in the visible and near infrared spectral regions*, Journal of Biomedical Photonics & Engineering, 4 (2018), p. 010503.

[64] J.-H. LEE, D.-H. KIM, H.-H. LEE, AND H.-W. KIM, *Role of nuclear mechanosensitivity in determining cellular responses to forces and biomaterials*, Biomaterials, 197 (2019), pp. 60–71.

[65] M. LEKKA, *Discrimination between normal and cancerous cells using AFM*, BioNanoScience, 6 (2016), pp. 65–80.

[66] P. LEMAITRE, M. BRUNEL, A. RONDEAU, E. PORCHERON, AND G. GRÉHAN, *Quasi real-time analysis of mixed-phase clouds using interferometric out-of-focus imaging: development of an algorithm to assess liquid and ice water content*, MeScT, 26 (2015), p. 125403.

[67] M. LI, L.-Q. LIU, N. XI, AND Y.-C. WANG, *Nanoscale monitoring of drug actions on cell membrane using atomic force microscopy*, Acta Pharmacologica Sinica, 36 (2015), pp. 769–782.

[68] Y. LI, A. MAHJOUBFAR, C. L. CHEN, K. R. NIAZI, L. PEI, AND B. JALALI, *Deep cytometry: Deep learning with real-time inference in cell sorting and flow cytometry*, Scientific Reports, 9 (2019), pp. 1–12.

[69] J. LIU, F. ZHANG, L. ZHU, X. QU, AND D. CHU, *Laser interference-based technique for dynamic measurement of single cell deformation manipulated by optical tweezers*, Electrophoresis, (2018).

[70] I. LÜCHTEFELD, A. BARTOLOZZI, J. MEJÍA MORALES, O. DOBRE, M. BASSO, T. ZAMBELLI, AND M. VASSALLI, *Elasticity spectra as a tool to investigate actin cortex mechanics*, Journal of Nanobiotechnology, 18 (2020).

[71] A. J. MACH, O. B. ADEYIGA, AND D. DI CARLO, *Microfluidic sample preparation for diagnostic cytopathology*, Lab on a Chip, 13 (2013), p. 1011.

[72] M. MATHELIÉ-GUINLET, A. T. ASMAR, J.-F. COLLET, AND Y. F. DUFRÊNE, *Lipoprotein lpp regulates the mechanical properties of the e. coli cell envelope*, Nature Communications, 11 (2020), pp. 1–11.

[73] A. MESCOLA, S. VELLA, M. SCOTTO, P. GAVAZZO, C. CANALE, A. DIASPRO, A. PAGANO, AND M. VASSALLI, *Probing cytoskeleton organisation of neuroblastoma cells with single-cell force spectroscopy*, Journal of Molecular Recognition, 25 (2012), pp. 270–277.

[74] A. MIETKE, O. OTTO, S. GIRARDO, P. ROSENDAHL, A. TAUBENBERGER, S. GOLFIER, E. ULBRICHT, S. ALAND, J. GUCK, AND E. FISCHER-FRIEDRICH, *Extracting cell stiffness from real-time deformability cytometry: Theory and experiment*, Biophysical Journal, 109 (2015), pp. 2023–2036.

[75] P. MISHRA, M. HILL, AND P. GLYNNE-JONES, *Deformation of red blood cells using acoustic radiation forces*, Biomicrofluidics, 8 (2014), pp. 1932–1058.

[76] M. MOKBEL, D. MOKBEL, A. MIETKE, N. TRÄBER, S. GIRARDO, O. OTTO, J. GUCK, AND S. ALAND, *Numerical simulation of real-time deformability cytometry to extract cell mechanical properties*, ACS Biomaterials Science & Engineering, 3 (2017), pp. 2962–2973.

[77] A. A. NAWAZ, M. URBANSKA, M. HERBIG, M. NÖTZEL, M. KRÄTER, P. ROSENDAHL, C. HEROLD, N. TOEPFNER, M. KUBÁNKOVÁ, R. GOSWAMI, S. ABUHATTUM, F. REICHEL, P. MÜLLER, A. TAUBENBERGER, S. GIRARDO, A. JACOBI, AND J. GUCK, *Intelligent image-based deformation-assisted cell sorting with molecular specificity*, Nature Methods, 17 (2020), pp. 595–599.

[78] O. OTTO, P. ROSENDAHL, A. MIETKE, S. GOLFIER, C. HEROLD, D. KLAUE, S. GIRARDO, S. PAGLIARA, A. EKPENYONG, A. JACOBI, M. WOBUS, N. TÖPFNER, U. F. KEYSER, J. MANSFELD, E. FISCHER-FRIEDRICH, AND J. GUCK, *Real-time deformability cytometry: on-the-fly cell mechanical phenotyping*, Nature Methods, 12 (2015), pp. 199–202.

[79] F. L. PEDROTTI, L. M. PEDROTTI, AND L. S. PEDROTTI, *Introduction to Optics*, Cambridge University Press, 3 ed., 2017.

[80] C. R. PFEIFER, C. M. ALVEY, J. IRIANTO, AND D. E. DISCHER, *Genome variation across cancers scales with tissue stiffness - an invasion-mutation mechanism and implications for immune cell infiltration*, Current Opinion in Systems Biology, 2 (2017), pp. 103–114.

[81] L. QIENI, J. WENHUA, L. TONG, W. XIANG, AND Z. YIMO, *High-accuracy particle sizing by interferometric particle imaging*, Optics Communications, 312 (2014), pp. 312–318.

[82] J. QIU, A. D. BAIK, X. L. LU, E. M. HILLMAN, Z. ZHUANG, C. DONG, AND X. E. GUO, *A noninvasive approach to determine viscoelastic properties of an individual adherent cell under fluid flow*, Journal of Biomechanics, 47 (2014), pp. 1537–1541.

[83] R. P. RAND AND A. C. BURTON, *Mechanical properties of the red cell membrane*, Biophysical Journal, 4 (1964), p. 115.

[84] M. J. ROSENBLUTH, W. A. LAM, AND D. A. FLETCHER, *Force microscopy of nonadherent cells: A comparison of leukemia cell deformability*, Biophysical Journal, 90 (2006), pp. 2994–3003.

[85] P. ROSENDAHL, K. PLAK, A. JACOBI, M. KRAETER, N. TOEPFNER, O. OTTO, C. HEROLD, M. WINZI, M. HERBIG, Y. GE, S. GIRARDO, K. WAGNER, B. BAUM, AND J. GUCK, *Real-time fluorescence and deformability cytometry*, Nature Methods, 15 (2018), pp. 355–358.

[86] C. ROTSCH AND M. RADMACHER, *Drug-induced changes of cytoskeletal structure and mechanics in fibroblasts: An atomic force microscopy study*, Biophysical Journal, 78 (2000), pp. 520–535.

[87] P. ROUHANI, S. HU, AND R. S. KIRSNER, *Melanoma in hispanic and black americans*, Cancer Control, 15 (2008), pp. 248–253.

[88] A. ROWAT, L. FOSTER, M. NIELSEN, M. WEISS, AND J. IPSEN, *Characterization of the elastic properties of the nuclear envelope*, Journal of The Royal Society Interface, 2 (2005), pp. 63–69.

[89] M. SARNA, A. ZADLO, B. CZUBA-PELECH, AND K. URBANSKA, *Nanomechanical phenotype of melanoma cells depends solely on the amount of endogenous pigment in the cells*, International Journal of Molecular Sciences, 19 (2018), p. 607.

[90] R. SCHAFER, *What is a savitzky-golay filter? [lecture notes]*, IEEE Signal Processing Magazine, 28 (2011), pp. 111–117.

[91] S. S. SHEVKOPLYAS, T. YOSHIDA, L. L. MUNN, AND M. W. BITENSKY, *Biomimetic autoseparation of leukocytes from whole blood in a microfluidic device*, Analytical Chemistry, 77 (2005), pp. 933–937.

[92] D. SHIN AND K. ATHANASIOU, *Cytoindentation for obtaining cell biomechanical properties*, Journal of Orthopaedic Research, 17 (1999), pp. 880–890.

[93] A. E. SIEGMAN, *Lasers*, University Science Books, 1986.

[94] A. E. SMITH, Z. ZHANG, C. R. THOMAS, K. E. MOXHAM, AND A. P. J. MIDDELBERG, *The mechanical properties of saccharomyces cerevisiae*, Proceedings of the National Academy of Sciences, 97 (2000), pp. 9871–9874.

[95] W. Z. SONG, X. M. ZHANG, A. Q. LIU, C. S. LIM, P. H. YAP, AND H. M. M. HOSSEINI, *Refractive index measurement of single living cells using on-chip fabry-pérot cavity*, Applied Physics Letters, 89 (2006), p. 203901.

[96] M. N. STARODUBTSEVA, *Mechanical properties of cells and ageing*, Ageing Research Reviews, 10 (2011), pp. 16–25.

[97] D. SUN, Y. RAN, AND G. WANG, *Label-free detection of cancer biomarkers using an in-line taper fiber-optic interferometer and a Fiber Bragg Grating*, Sensors, 17 (2017), p. 2559.

[98] S. SURESH, *Biomechanics and biophysics of cancer cells*, Acta Biomaterialia, 3 (2007), pp. 413–438.

[99] J. SWIFT, I. L. IVANOVSKA, A. BUXBOIM, T. HARADA, P. C. D. P. DINGAL, J. PINTER, J. D. PAJEROWSKI, K. R. SPINLER, J.-W. SHIN, M. TEWARI, F. REHFELDT, D. W. SPEICHER, AND D. E. DISCHER, *Nuclear lamin-a scales with tissue stiffness and enhances matrix-directed differentiation*, Science (New York, N.Y.), 341 (2013), p. 1240104.

[100] I. TITUSHKIN AND M. CHO, *Distinct membrane mechanical properties of human mesenchymal stem cells determined using laser optical tweezers*, Biophysical Journal, 90 (2006), pp. 2582–2591.

[101] W. R. TRICKEY, G. M. LEE, AND F. GUILAK, *Viscoelastic properties of chondrocytes from normal and osteoarthritic human cartilage*, Journal of Orthopaedic Research, 18 (2000), pp. 891–898.

[102] M. URBANSKA, P. ROSENDAHL, M. KRÄTER, AND J. GUCK, *Chapter 10- high throughput single-cell mechanical phenotyping with real-time deformability cytometry*, 01 2018.

[103] M. URBANSKA, M. WINZI, K. NEUMANN, S. ABUHATTUM, P. ROSENDAHL, P. MÜLLER, A. TAUBENBERGER, K. ANASTASSIADIS, AND J. GUCK, *Single-cell mechanical phenotype is an intrinsic*

marker of reprogramming and differentiation along the mouse neural lineage, Development, 144 (2017), pp. 4313–4321.

[104] S. C. UZOECHI AND N. I. ABU-LAIL, *Changes in cellular elasticities and conformational properties of bacterial surface biopolymers of multidrug-resistant escherichia coli (MDR-E. coli) strains in response to ampicillin*, The Cell Surface, 5 (2019), p. 100019.

[105] P. A. VALBERG, *Magnetometry of ingested particles in pulmonary macrophages*, Science, 224 (1984), pp. 513–516.

[106] S. VAN DER WALT, J. L. SCHÖNBERGER, J. NUNEZ-IGLESIAS, F. BOULOGNE, J. D. WARNER, N. YAGER, E. GOUILLART, T. YU, AND THE SCIKIT-IMAGE CONTRIBUTORS, *scikit-image: image processing in Python*, PeerJ, 2 (2014), p. e453.

[107] P. VIRTANEN, R. GOMMERS, T. E. OLIPHANT, M. HABERLAND, T. REDDY, D. COURNAPEAU, E. BUROVSKI, P. PETERSON, W. WECKESSER, J. BRIGHT, S. J. VAN DER WALT, M. BRETT, J. WILSON, K. J. MILLMAN, N. MAYOROV, A. R. J. NELSON, E. JONES, R. KERN, E. LARSON, C. J. CAREY, İ. POLAT, Y. FENG, E. W. MOORE, J. VANDERPLAS, D. LAXALDE, J. PERKTOLD, R. CIMRMAN, I. HENRIKSEN, E. A. QUINTERO, C. R. HARRIS, A. M. ARCHIBALD, A. H. RIBEIRO, F. PEDREGOSA, P. VAN MULBREGT, AND SCIPY 1.0 CONTRIBUTORS, *SciPy 1.0: Fundamental Algorithms for Scientific Computing in Python*, Nature Methods, 17 (2020), pp. 261–272.

[108] D. V. VORONIN, A. A. KOZLOVA, R. A. VERKHOVSKII, A. V. ERMAKOV, M. A. MAKARKIN, O. A. INOZEMTSEVA, AND D. N. BRATASHOV, *Detection of rare objects by flow cytometry: Imaging, cell sorting, and deep learning approaches*, International Journal of Molecular Sciences, 21 (2020).

[109] B.-T. WANG AND Q. WANG, *An interferometric optical fiber biosensor with high sensitivity for igg/anti-igg immunosensing*, Optics Communications, 426 (2018), pp. 388–394.

[110] H. WANG, Z. LIU, D. M. SHIN, Z. G. CHEN, Y. CHO, Y.-J. KIM, AND A. HAN, *A continuous-flow acoustofluidic cytometer for single-cell mechanotyping*, Lab on a Chip, 19 (2019), pp. 387–393.

[111] P.-H. WU, D. R.-B. AROUSH, A. ASNACIOS, W.-C. CHEN, M. E. DOKUKIN, B. L. DOSS, P. DURAND-SMET, A. EKPENYONG, J. GUCK, N. V. GUZ, P. A. JANMEY, J. S. H. LEE, N. M. MOORE, A. OTT, Y.-C. POH, R. ROS, M. SANDER, I. SOKOLOV, J. R. STAUNTON, N. WANG, G. WHYTE, AND D. WIRTZ, *A comparison of methods to assess cell mechanical properties*, Nature Methods, 15 (2018), pp. 491–498.

[112] X. WU, Z. SUN, A. FOSKETT, J. P. TRZECIAKOWSKI, G. A. MEININGER, AND M. MUTHUCHAMY, *Cardiomyocyte contractile status is associated with differences in fibronectin and integrin interactions*, American Journal of Physiology - Heart and Circulatory Physiology, 298 (2010), pp. H2071–H2081.

[113] L. WULLKOPF, A.-K. V. WEST, N. LEIJNSE, T. R. COX, C. D. MADSEN, L. B. ODDERSHEDE, AND J. T. ERLER, *Cancer cells' ability to mechanically adjust to extracellular matrix stiffness correlates with their invasive potential*, Molecular Biology of the Cell, 29 (2018), pp. 2378–2385.

[114] Y. ZHAN, D. N. LOUFAKIS, N. BAO, AND C. LU, *Characterizing osmotic lysis kinetics under microfluidic hydrodynamic focusing for erythrocyte fragility studies*, Lab on a Chip, 12 (2012), pp. 5063–5068.

[115] H. ZHANG, X. WANG, J. SUN, D. JIA, AND T. LIU, *Multidispersed bubble-size measurements by interferometric particle imaging at scattering angles of 90° and 45°*, Applied Optics, 57 (2018), pp. 10496–10504.

[116] Y. ZHENG, J. NGUYEN, Y. WEI, AND Y. SUN, *Recent advances in microfluidic techniques for single-cell biophysical characterization*, Lab on a Chip, 13 (2013), pp. 2464–2483.

[117] R. ZHU, T. AVSIEVICH, A. POPOV, AND I. MEGLINSKI, *Optical tweezers in studies of red blood cells*, Cells, 9 (2020).

[118] R. ZMIJAN, U. S. JONNALAGADDA, D. CARUGO, Y. KOCHI, E. LEMM, G. PACKHAM, M. HILL, AND P. GLYNNE-JONES, *High throughput imaging cytometer with acoustic focussing*, RSC Adv., 5 (2015), pp. 83206–83216.

Acronyms

A

AFM Atomic Force Microscopy 19–21, 27, 30, 33, 97, 98
AIC Acoustofluidic Interferometric Cytometry 35, 96
AID Acoustofluidic Interferometric Device 33, 35, 37, 56, 67, 68, 72, 83–86, 91, 92, 94, 97–100, 102, 103, 117
AIT Acoustofluidic Interferometric Technique 85, 96–98, 100, 101
ANOVA Analysis of Variance 81, 84

B

BALB/3T3 Mouse Fibroblast 97
BFA Bare Fiber Adapter 11
BT-474 Human Mammary Gland Carcinoma 25, 26

C

CD34+ Transmembrane Phosphoglycoprotein Protein 28
CFL Cell Focal Length 35, 55, 59, 68, 77, 78, 80–90, 102
CFPP Cell-Induced Fringe Pattern Perturbation 67–69, 72–78, 80, 81, 83, 84, 89, 92–95, 102, 103, 125
CFU Colony Forming Units 10
cl-37B Human Neck Cancer Cell Line 25, 27
CMOS Complementary Metal Oxide Semiconductor 10, 28, 30
CMR Cell Monolayer Rheology 19, 21

D

DDS Direct Digital Synthesizer 36, 40
DNA Deoxyribonucleic Acid 97
DWT Discrete Wavelet Transform 18

E

ECM Extracellular Matrix 21, 96

F

F-actin Filamentous actin 99
FACS Fluorescence-Activated Cell Sorting 101
FFPE Formalin-Fixed Paraffin-Embedded 11
fNPCs Murine Fetal Neural Progenitor Cells 17
FOV Field of View 72
FP Fabry-Perot 8, 10, 35, 50–52, 57, 69, 70
FSR Free Spectral Range 7, 32, 53, 68, 72, 73, 75, 78, 84, 92
FWHM Full-Width at Half-Maximum 7, 8, 32, 53, 68, 72, 73, 75, 78, 84, 92, 93, 95

G

GFP Green Fluorescent Protein xviii, 10, 100
GPCR G-protein Coupled Receptor 91

H

HEK293 Human Embryonic Kidney 293 Cells xviii, 10, 100
HeLa Cervical Epithelial Cell Line 10
HER2 Human Epidermal Growth Factor Receptor 2 17
HS Hereditary Spherocytosis 98
HWHM Half-Width at Half-Maximum 8

I

IM Interferometric Microscopy 9
iPSCs Induced Pluripotent Stem Cells 17

L

LED Light Emitting Diode 28
Lpp Lipoprotein 101

M

MβCD Methyl-β-cyclodextrins 12
M4e Human Neck Cancer Cell Line 25, 27
MA Micropipette Aspiration 19–21, 30
MCF-10A Human Mammary Gland Cell Line 25–27
MCF7 Human Mammary Gland Adenocarcinoma 25–27
MDA-MB-231 Human Mammary Gland Adenocarcinoma 25–27
MR Microbead Rheometry 19
MscL Large Conductance Mechanosensitive Ion Channel 100

O

OTs Optical Tweezers and Traps 19, 21, 22, 30

P

PDMS Polydimethylsiloxane 101
Pf Plasmodium falciparum 98
PIEZO1 PIEZO1 Gene/Mechanosensitive Channel 100
PM Plasma Cell Membrane 15

R

RBC Red Blood Cells 9, 15, 20, 22, 28, 30, 31, 97, 98, 102
RFP Resonator Fringe Pattern 37, 39, 50, 55, 68–72, 74, 75, 95
RI Refractive Index 9, 10, 12, 15, 17
RIU Refractive Index Units 10
RT-DC Real-Time Deformability Cytometry 28, 42, 92

S

SAW Surface Acoustic Wave 24
SCD Sickle Cell Disease 23, 24
SGF Savitzky–Golay Filter 76, 93, 125
SMF Single Mode Fiber 11
SV-T2 Mouse Malignal Fibroblast 97

T

Tu686 Human Neck Cancer Cell Line 25, 27

W

WBC White Blood Cell 30, 102

Patent

- 2020, Julián Mejía, Gian Luca Lippi and Massimo Vassalli. *Optoacoustic monitoring device for cell characterization*, EP20306149, filed to the European Patent office.

Publications

- To apply for the patent, the technology in this thesis was subjected to secrecy, preventing its publication in scientific articles. The condition of secrecy was removed in October 2020 by the French Defence Department. Scientific publications are under preparation.

Related publications

Publications on related subjects and developed in parallel with the AID project.

- 2021, Julián Mejía Morales, Björn Hammarström, Gian Luca Lippi, Peter Glynne-Jones and Massimo Vassalli. *Acoustic focusing enables registration-free in-chip quantitative phase imaging*, Biomicrofluidics. (15), 014102, https://doi.org/10.1063/5.0036585

- 2020, Ines Lüchtefeld, Alice Bartolozzi, Julián Mejía Morales, Michele Basso, Tomaso Zambelli, and Massimo Vassali. *Single Cell Elasticity Spectra provide insights into the Actin Cortex Mechanics and Thickness*, Nanobiotechnology Journal. 1(18) 147, https://doi.org/10.1186/s12951-020-00706-2

Conferences

- 2020, Biophysical Society Meting 2020 **(USA)**, Contributed presentation: *Acoustofluidic Interferometric Techniques For Singel Cell Optical Phenotyping* **Link to presentation**

- 2018, Simposio Becarios CONACyT en Europa **(FRANCE)**, Poster: *Fabry-Perot interferometer with aqueous etalon and its possible application in microbiology*

Workshops

- 2019, Cote d'Azur International Workshop on Cell Mechanics Advanced Tools and Applications to Biomedical Problems **(FRANCE)**, Poster: *Cells Quantitative 3D profile by means of the Transport of Intensity Equation using Rigid Registration*

- 2019, Complex Days Université Côte d'Azur **(FRANCE)**, Poster: *Detection Methods of Cell Deformability*
- 2018, International Biophysical School "Academician Radoslav K. Andjus" (NERKA) **(MONTENEGRO)**
- 2018, Thematic days on Fluids and Complexity "Interfaces" **(FRANCE)**, Poster: *Detection Methods of Cell Deformability*
- 2018, Nanoengineering For Mechanobiology **(ITALY)**. Poster: *Fabry-Perot interferometer with aqueous etalon and its possible application in microbiology*

Real time analysis resonances time traces Python script. Code working for the oscilloscope DSOX 3062 A

Fringe patterns time traces analysis

```
#! /usr/bin/env python
#This code combines jetdsox2.py with gneral_traces.py
###11-03-2019
##---------- Instantiation DSOX.py ----------##
##-- To get the signal from a Keysight InfiniiVision 3000 --##

"""SYNOPSIS:
getdso [OPTIONS]... STRING
DESCRIPTION:
Get time traces in STRING from the Agilent DSO-X scopes.
ARGUMENTS:
STRING are channels the you want to get in a coma separated list.
Channels have to be written C1 or C2 etc.
For example getdso c1,c2 to get channels 1 and 2 and
print them to stdout
OPTIONS:
-h, --help
-o file,
--output=file
-F, --Force
Display this help
Send data to "file". Data will be written
in binary form. By default, an existing file
will NOT be overwritten. '.chX' will be
added as extension, where X is channel number.
Force overwrite existing files.
-i address,
--ip=address
Set the IP address of the device.
-P, --Plot
Plot the data (only 10 000 points, evenly spaced,
will be shown).
EXAMPLES:
Return traces 1 and 2 as columns of 8 bits unsigned integer numbers
and print them to stdout:
$ getdso c1,c2
Get traces from channel 1 and channel 2, plot them and write them
to files datafile.C1 and datafile.C2. Files are overwritten if
they exist:
$ getdso -o datafile -P -F c1,c2
```

```
"""

__version__ = "$Revision: 0.1 $"
import sys
import getopt
from DSOX import DSOX
import numpy as np
import os
import re
import instruments_common as ic
import time
import matplotlib.pyplot as plt
from scipy.signal import savgol_filter as sg
from scipy.signal import find_peaks
from scipy.stats import signaltonoise

def find_nearest(array, value):
    array = np.asarray(array)
    idx = (np.abs(array - value)).argmin()
return idx

def main(module):
    """Uses the DSOX module to drive the scope.
    Scope is first set to STOP if needed, then trace(s) are acquired
    and printed to stdout
    """
    error = 0
    force = 0
    outfile = None
    logfile = 1
    plot=False
    # parse command line options
    try:
        opts, args = getopt.getopt(sys.argv[1:],
        "Fho:li:P", ["Force","help",
        "output=","logfile","ip=","Plot"])
    except getopt.error, msg:
        print msg
        print "for help use --help"
        sys.exit(2)
# process options
for option, argument in opts:
    if option in ("-h", "--help"):
        print __doc__
        sys.exit(0)
    if option in ("-F", "--Force"):
        force = 1
    if option in ("-P", "--Plot"):
        plot = True
if option in ("-o", "--output"):
    if argument=='':
        print "Give a name for the output file"
        sys.exit(0)
```

```
            outfile = argument
        if option in ("-i","--ip"):
            if argument=='':
            print "Option -i --ip needs an argument"
            sys.exit(0)
        host = argument
    # process arguments
    if len(args) == 0:
        print sys.argv[0], "needs an argument."
        print "for help use --help"
        sys.exit(0)
    # put argument list in good shape
    channels = args[0].upper()
    channels = re.sub('C','CHAN',channels)
    # initialize
    scope = module(host)
    channels = channels.split(',')
    #for j in range(2):
    #get data
    #channels = channels.split(',')
    data, logs = scope.get_traces(channels, get_logs=True)

    ##----------- Traces Analysis ----------##
    ##--------------------------------------##
    time_gap=[]
    y_gap=[]
    for d in data[:]:
        i = 1
        # Reshape the arrays containing the data frome each channel
        size = len(d)
        x = np.arange(size).reshape((size,1))
        y = d.reshape(size,1).astype('float')
        x1 = x[:,0]
        y1 = y[:,0]
    # Reducing the amount of points in the data array no more than 6000
    while len(y1) > 6000:
        y1 = y1[0::2]
        x1 = x1[0::2]
    #Ploting the raw signal
    plt.subplot(311)
    plt.plot(x1,y1,'ko')
    # Setting the window size for the Savizky-Golay filter
    # as fraction of the total of points in the array y1
    # w1 = 801 A value that fits ok the data from "reduced-36.csv"
    w1 = int(len(y1)//4.5)
    #Ensuring w1 is an odd number
    if (w1 % 2) == 0 :
    w1 = w1 + 1
    # Calculation of the SG filter
    # Strong filter to remove all the noise leaving only the general behaviour
    # yraw = sg(y1,801,3)
    yraw = sg(y1,int(w1),3)
    #Inrverting the signal to get the valleys
```

```
y_inversed = 1-yraw
max_raw = np.max(y_inversed)
min_raw = np.min(y_inversed)
# Setting the parameters for valleys detection as proportions
# The valleys that are larger than oner quarter of the difference
# between maximum and minum value of the data and are below the average of
#the data will be detected
threshold_1 = (max_raw - min_raw) / 2 + min_raw
threshold_2 = abs(max_raw - threshold_1) / 2
max_x = np.max(x1)
min_x = np.min(x1)
valleys = find_peaks(y_inversed, height = threshold_1, prominence =
threshold_2 , distance = None )[0]
plt.plot(x1[valleys],yraw[valleys],'mo',ms=5)
plt.plot(x1,yraw,'b-')
# Filtering the data with SG filter and taking the second derivative
# to find peaks in the inflection points
# the criteria is that the peaks are above the average between the max and
#min in the array
# and has an height of at least one eighth of difference between max and
#min
y_pro = 1-sg(yraw,int(w1),3,deriv=2)
max_pro = np.max(y_pro)
min_pro = np.min(y_pro)
threshold_1 = (max_pro - min_pro) / 2 + min_pro
threshold_2 = abs(max_pro - threshold_1) / 4
plt.subplot(312)
plt.plot(x1,y_pro,'r-')
gminima = find_peaks(y_pro, height = threshold_1 , prominence =
threshold_2 )[0]
plt.subplot(312)
plt.plot(x1[gminima],y_pro[gminima],'ko',ms=5)
borders = []
min_vall = []
# Once detected the valleys and the inflection points
# the consective inflection points (gminima) having a valley
# in between are identified as full valleys
for i in range(len(valleys)):
    for j in range(len(gminima)):
        if (j+1) <= len(gminima):
            if x1[valleys[i]] > x1[gminima[j]] and x1[valleys[i]] < x1
                [gminima[j+1]]:
                borders.append(gminima[j])
                borders.append(gminima[j+1])
                min_vall.append(valleys[i])
                plt.subplot(311)
                plt.plot(x1[borders],yraw[borders],'ro',ms=5)
# Identify putative borders of valleys
nfullvalleys = int(np.floor(len(borders)/2))
# After identifying the full valleys an analysis of the maxima and minima
in the valleys are computed
# A softer SG filter (leaving the data less filtered) is used, meaning a
smaller window w2
```

```
w2 = np.floor(len(y1) / 20)
#w2 = np.floor(len(y1) / 10)
#print w2
if (w2 % 2) == 0 :
w2 = w2 + 1
#print int(w2), len(y1)
#yfine = sg(y1,201,3)
yfine = sg(y1,int(w2),3)

#For each of the full valleys a search for peaks, min and max is started
#it is consider the valley within the putative borders
#within the valley the criteria for find peaks are that
#it must be abobe the tenth of the difference between max an min value
#and it must has a minimum of a 20th of such difference
#same criteria for the minimun but the data is inverted as before in find
#valleys

for val in range(nfullvalleys):
    ileft = int(borders[2*val])
    iright = int(borders[2*val+1])
    yval = yfine[ileft:iright]
    plt.subplot(313)
    plt.plot(x1[ileft:iright],yval,'b-')
    max_val = np.max(yval)
    min_val = np.min(yval)
    threshold_1 = (max_val - min_val) / 10 + min_val
    threshold_2 = abs(max_val - threshold_1) / 10
    imaxima = find_peaks(yval,height = threshold_1 ,prominence =
    threshold_2)[0]+ileft
    plt.subplot(313)
    plt.plot(x1[imaxima],yfine[imaxima],'ro',ms=10)
    yval_invert = 1 - yval
    max_val_i = np.max(yval_invert)
    min_val_i = np.min(yval_invert)
    threshold_1i = (max_val_i - min_val_i) / 10 + min_val_i
    threshold_2i = abs(max_val_i - threshold_1i) / 10
    iminima = find_peaks(yval_invert,height = threshold_1i ,prominence =
    threshold_2i)[0]+ileft
    plt.subplot(313)
    plt.plot(x1[iminima],yfine[iminima],'go',ms=10)
# Here the FWHM is detected and measured for each full valley found
# The average of the heigth of the borders is consider the base of the
#valley
# The half is determined as the half difference between the base and
#the peak
# consider as maxima in full valleys
ybase = (yraw[ileft] + yraw[iright])/2
ycima = yraw[min_vall[val]]
halfmaximum = (ybase-ycima)/2 + ycima

# The closest value to the Half Maxima (halfmaximum) of the raw filter
#is located
# For each side of the valley
```

```
    xai = find_nearest(yraw[ileft:min_vall[val]], halfmaximum)
    xbi = find_nearest(yraw[min_vall[val]:iright], halfmaximum)
    xa = x1[xai + ileft]
255 xb = x1[xbi + min_vall[val]]
    plt.subplot(311)
    plt.plot([xa,xb],[halfmaximum,halfmaximum],'yo-',ms=5)
    print("The FWHM of the valley",val+1,"is",abs(xa-xb))
    window_time = 50e-3
260 oscilloscope = len(y)
    scale = window_time/oscilloscope
    print('Considering a time window of ', window_time, 'ms in the
    oscilloscope the FWHM are',val+1, abs(xa-xb)*scale )
    #plt.subplot(311)
265 #plt.plot(x[time_gap],y_gap,'go',ms=10)
    #print 'The time gap is',abs(time_gap[1]-time_gap[0])
    plt.show()
    #print j
    #time.sleep(0.5)
270 #print datxy
    #np.savetxt("tj1.csv", datxy, delimiter=",",fmt='%1.5i')

    if __name__ == "__main__":
    module = DSOX
275 main(module)
```

Performance of the code

The DSOXJ.py code, useful to acquire and analyze the CFPP in real-time, is tested here. Different features in the time traces may affect the code,Äôs performance. Ideally, only one event will occur in the observation time frame. Nevertheless,if more than one event occurs, the code is designed to analyze each event's events. Moreover, events with different magnitude, shortly spaced in time (cf. Figs. (A1) and (A2),) or too close to the time frame boundaries (cf. Fig. (A3)) might lead to erroneous results in the analysis. The effect of the Savitzky−Golay Filter (SGF) on the performance of the code is also presented (cf. Figs. (A4) and (A5)) on synthetically generated data.

The window_length w_1 (or the number of coefficients) is the parameter used in the SGF to control the smoothness of the data [107]. Small window_length w_1 values leave the data unchanged, while w_1 values in the order of hundreds will have a strong data smoothing effect. Notice that the window length must be a positive odd integer.

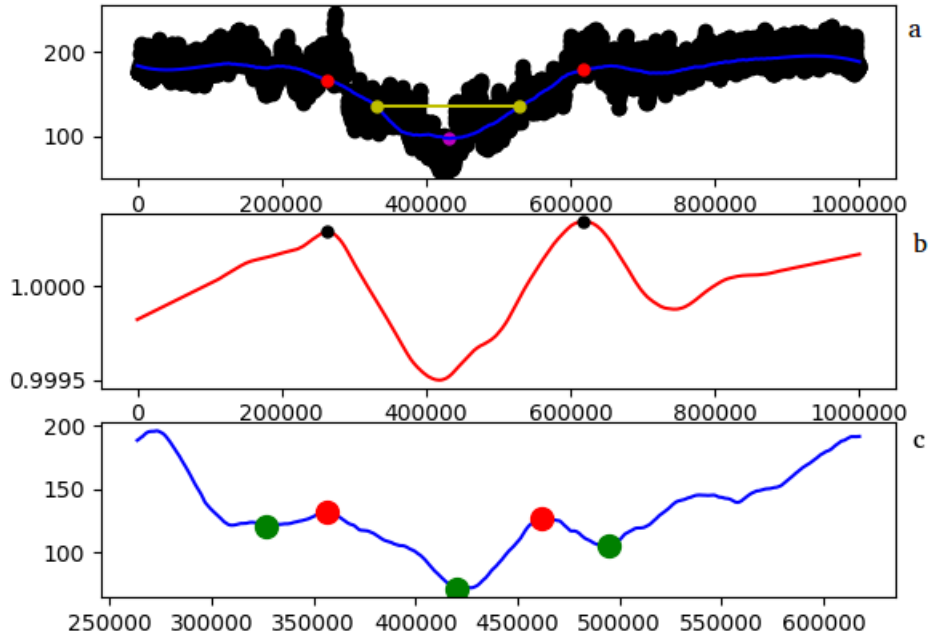

FIGURE A1. Time trace with only one well-defined particle. a) In black the raw time trace,n blue the SG-filtered data with a window of ($w_1 = 801$), in purple the min of the found valley, in red the inflection points that serve as borders of the valley. b) The SG-filtered data with the same window but taking the second derivative to highlight the inflection points, the black points mark the identified inflection points, which serve as valley borders in a) (red dots). c) The blue line is the portion of the filter signal corresponding to the valley. The peaks are shown in red if they are maxima and in green, if they are minima.

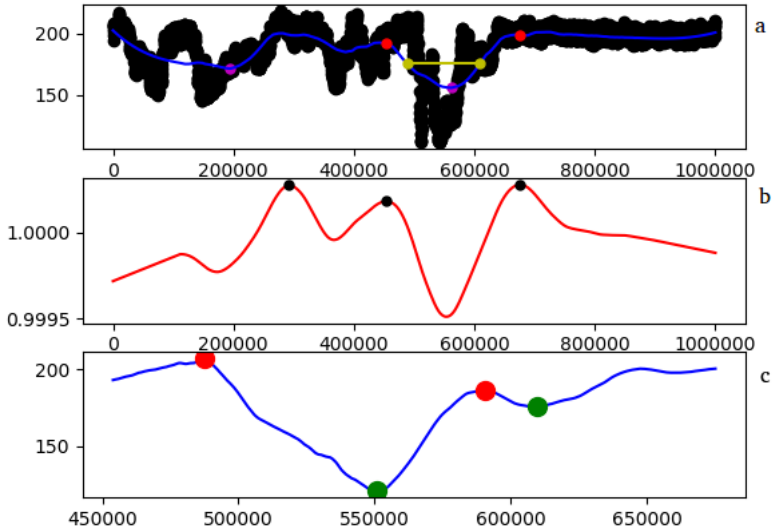

FIGURE A2. Time trace with two valleys but only one-well-defined particle. a) In black the raw time trace,n blue the SG-filtered data with a window of ($w_1 = 801$), in purple the min of the found valley, in red the inflection points that serve as borders of the valley. b) The SG-filtered data with the same window but taking the second derivative to highlight the inflection points, the black points mark the identified inflection points, which serve as valley borders in a) (red dots). c) The blue line is the portion of the filter signal corresponding to the valley. The peaks are shown in red if they are maxima and in green, if they are minima.

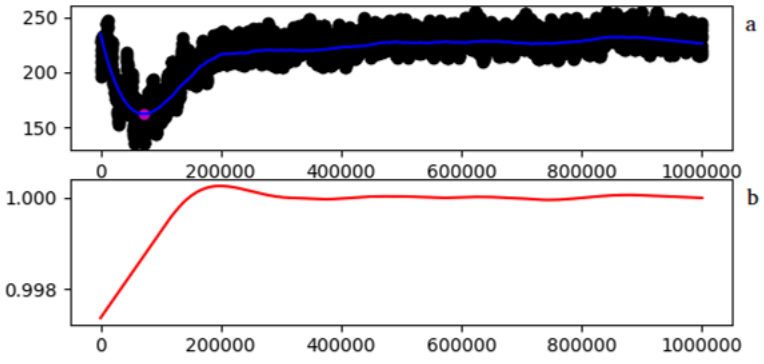

FIGURE A3. Visual inspection shows the presence of a particle, but the algorithm has difficulties recognizing it because of its closeness to the trace's border. a) In black the raw time trace,n blue the SG-filtered data with a window of ($w_1 = 801$), in purple the min of the found valley, in red the inflection points that serve as borders of the valley. b) The SG-filtered data with the same window but taking the second derivative to highlight the inflection points, no points are identified.

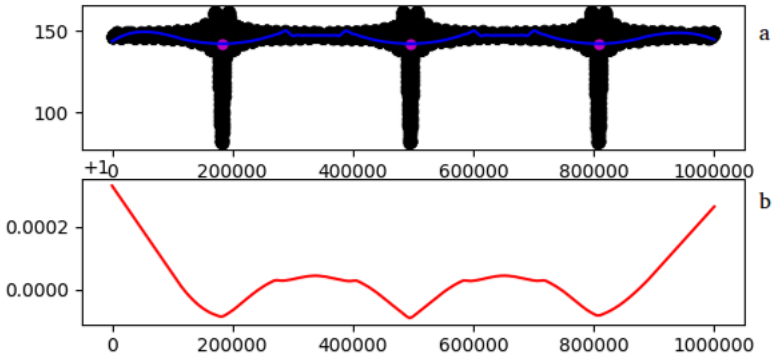

FIGURE A4. Time trace of inverse cardinal sine imitating a well-defined particle signal with low noise. The program fails to detect the information because the SF filter is used on a window width of ($w_1 = 801$) which is excessive compared to the signal's structure. a) In black the raw time trace, in blue the SG-filtered data, in purple the min of the found valley, in red the inflection points that serve as borders of the valley. b) The SG-filtered data with the same window but taking the second derivative to highlight the inflection points, no points are identified.

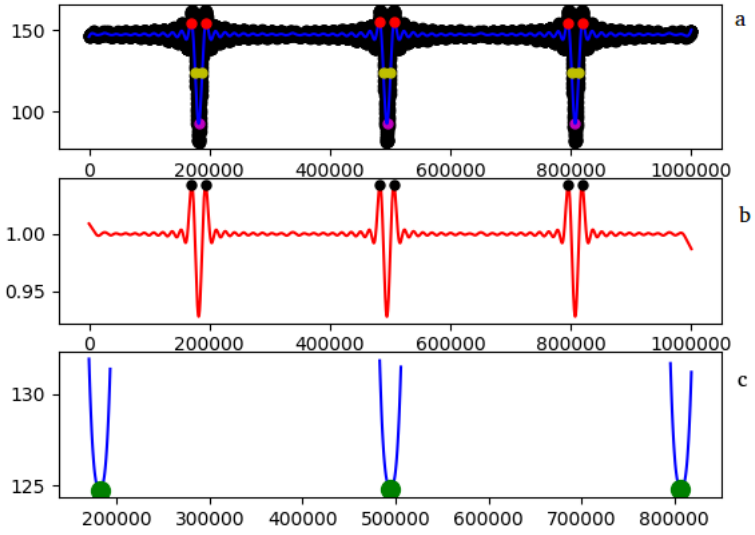

FIGURE A5. Time trace of inverse cardinal sine imitating a well-defined particle signal with low noise, with a low SG filter the program is working well. a) In black the raw time trace, in blue the SG-filtered with a window of ($w_1 = 401$), in purple the min of the found valley, in red the inflection points that serve as borders of the valley. b) The SG-filtered data with the same window but taking the second derivative to highlight the inflection points, the black points mark the identified inflection points, which serve as valley borders in a) (red dots). c) The blue line is the portion of the filter signal corresponding to the full valleys. The peaks are shown in green since there are only minima.